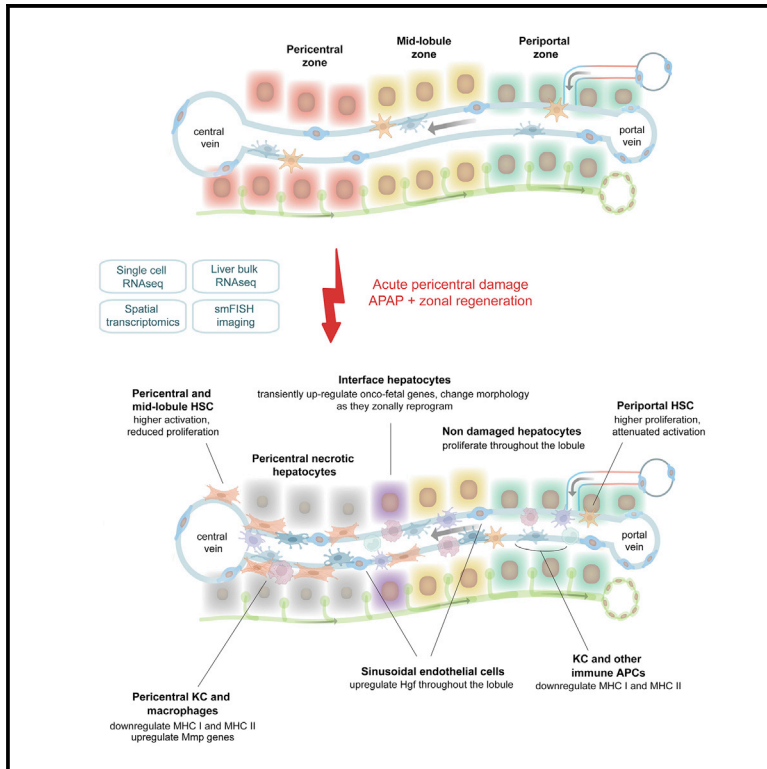


Cell Stem Cell

The spatiotemporal program of zonal liver regeneration following acute injury

Graphical abstract



Authors

Shani Ben-Moshe, Tamar Veg,
Rita Manco, ..., Keren Bahar Halpern,
Eran Elinav, Shalev Itzkovitz

Correspondence

shalev.itzkovitz@weizmann.ac.il

In brief

Ben-Moshe et al. study the rapid process of liver regeneration following acute drug-induced pericentral damage.

Hepatocytes proliferate throughout the lobule to rapidly generate missing cells. Incoming pericentral hepatocytes change morphology, elevate protein turnover, and upregulate oncofetal genes as they zonally reprogram. Nonparenchymal cells orchestrate the process by zone-dependent cues.

Highlights

- Spatiotemporal liver cell atlas of zonal regeneration following acute APAP injury
- New pericentral hepatocytes express onco-fetal genes while zonally reprogramming
- Nonparenchymal cells exhibit zone-specific cues to instruct regeneration
- Global reduction in MHC-I genes may prevent induction of adaptive immunity



Resource

The spatiotemporal program of zonal liver regeneration following acute injury

Shani Ben-Moshe,¹ Tamar Veg,¹ Rita Manco,¹ Stav Dan,¹ Delfina Papinutti,¹ Aviezer Lifshitz,² Aleksandra A. Kolodziejczyk,³ Keren Bahar Halpern,¹ Eran Elinav,^{3,4} and Shalev Itzkovitz^{1,5,*}

¹Department of Molecular Cell Biology, Weizmann Institute of Science, Rehovot, Israel

²Department of Computer Science and Applied Mathematics and Department of Biological Regulation, Weizmann Institute, Rehovot, Israel

³Systems Immunology Department, Weizmann Institute of Science, Rehovot, Israel

⁴Microbiome & Cancer Division, DKFZ, Heidelberg, Germany

⁵Lead contact

*Correspondence: shalev.itzkovitz@weizmann.ac.il

<https://doi.org/10.1016/j.stem.2022.04.008>

SUMMARY

The liver carries a remarkable ability to regenerate rapidly after acute zonal damage. Single-cell approaches are necessary to study this process, given the spatial heterogeneity of liver cell types. Here, we use spatially resolved single-cell RNA sequencing (scRNA-seq) to study the dynamics of mouse liver regeneration after acute acetaminophen (APAP) intoxication. We find that hepatocytes proliferate throughout the liver lobule, creating the mitotic pressure required to repopulate the necrotic pericentral zone rapidly. A subset of hepatocytes located at the regenerating front transiently upregulate fetal-specific genes, including *Afp* and *Cdh17*, as they reprogram to a pericentral state. Zonated endothelial, hepatic stellate cell (HSC), and macrophage populations are differentially involved in immune recruitment, proliferation, and matrix remodeling. We observe massive transient infiltration of myeloid cells, yet stability of lymphoid cell abundance, in accordance with a global decline in antigen presentation. Our study provides a resource for understanding the coordinated programs of zonal liver regeneration.

INTRODUCTION

The liver is a highly heterogeneous organ. Hepatocytes and supporting nonparenchymal cells operate in repeating hexagonally shaped anatomical units termed “liver lobules.” Blood enters the lobules at their corners, termed “portal nodes,” and flows inward through sinusoidal channels into draining central veins (CVs). This polarized blood flow, in conjunction with sequential consumption and secretion of hepatocytes, generates gradients of oxygen, nutrients, and hormones. The gradients of blood-borne factors and additional morphogen gradients create a highly heterogeneous microenvironment. As a result, cells at different lobule coordinates exhibit notable differences in gene expression, a phenomenon termed “liver zonation” (Ben-Moshe and Itzkovitz, 2019; Gebhardt, 1992; Jungermann and Keitzmann, 1996). About half of the hepatocyte genes are zoned, with processes such as gluconeogenesis, and protein secretion allocated to the periportal hepatocytes and other processes such as drug detoxification allocated to pericentral hepatocytes (Halpern et al., 2017). Liver endothelial cells (Halpern et al., 2018; Inverso et al., 2021) and hepatic stellate cells (HSCs) (Dobie et al., 2019) exhibit similar broad functional zonation patterns along the lobule radial axis. It is unclear how this spatial heterogeneity affects liver pathology and regeneration processes.

The liver exhibits robust regenerative capacity (Michalopoulos and DeFrances, 1997). In response to acute doses of drugs, such as acetaminophen (APAP, Bhushan and Apte, 2019; Mossa-

nen and Tacke, 2015) or CCl₄ (Recknagel, 1967), pericentral hepatocytes that attempt to detoxify these foreign substances are overwhelmed with toxic intermediates and die. The remaining liver tissue enters a regenerative mode, leading to rapid healing and replacement of the damaged lobule layers (Yanger et al., 2014). Zonal regeneration involves a coordinated set of processes that have to be carried out in the right place and time. Dead hepatocytes need to be efficiently cleared, while preventing induction of the adaptive immune system exposed to the multiple new available antigens. Extracellular matrix needs to be constructed rapidly to support the tissue scaffold, yet disintegrated once new cells are formed, to prevent lasting fibrosis (Adler et al., 2020; Kisseleva and Brenner, 2006). Most importantly, hepatocytes originating in lobule zones with profoundly different expression signatures need to be rapidly generated and reprogrammed to take over the critical pericentral hepatocyte functions. Single-cell approaches have been used to study nonparenchymal cells during the acute phase of APAP intoxication at 20 h after damage (Kolodziejczyk et al., 2020); however, the spatial and temporal dynamics of the coordinated response of all liver cell types across the entire zonal regeneration process have not been explored.

RESULTS

A single-cell atlas of zonal regeneration after APAP

To study zonal regeneration, we injected mice with an acute dose of 300 mg/kg APAP (Figure 1A) and sampled livers at different



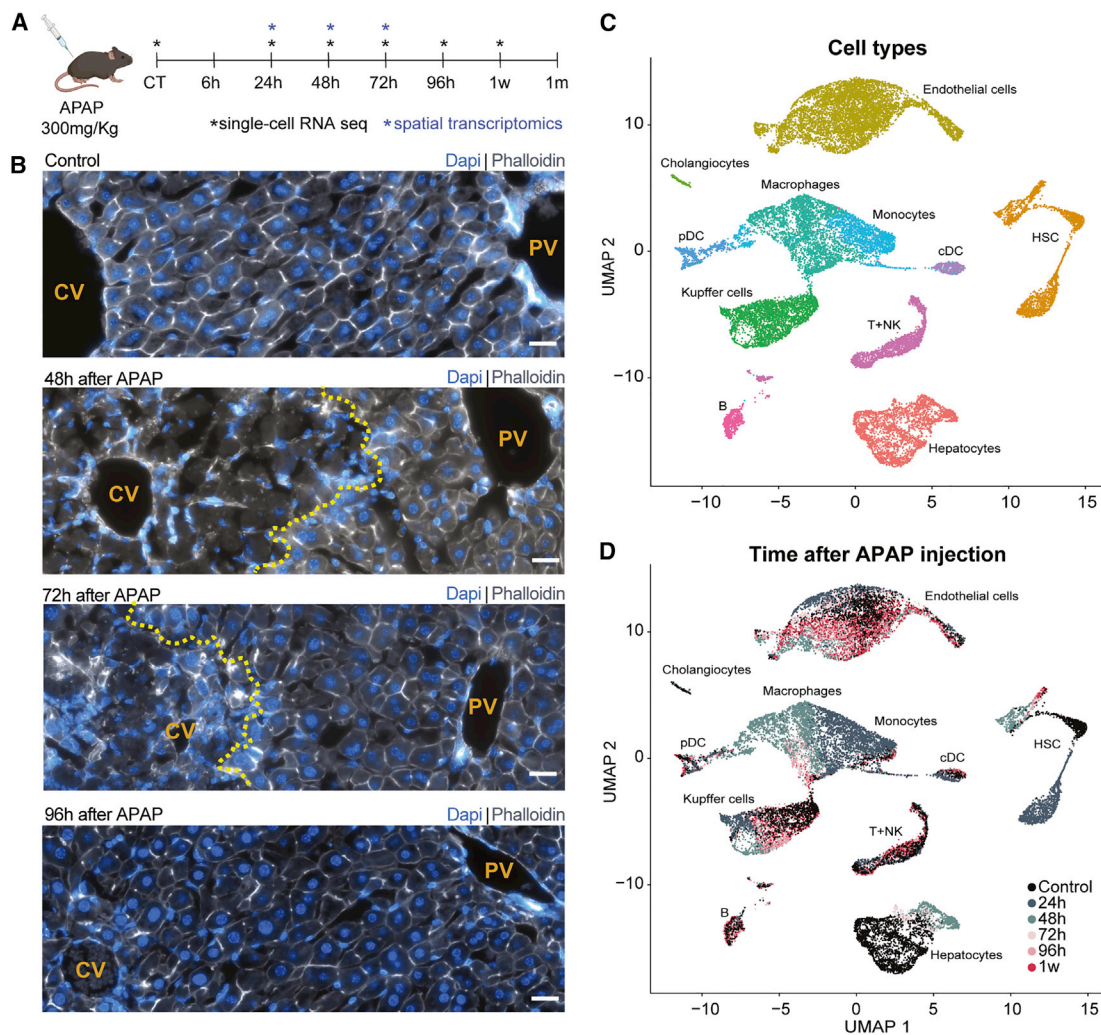


Figure 1. Acute dose of APAP induces liver damage and regeneration

(A) A schematic of the experimental design. Mice were injected with 300 mg APAP/1 kg body weight. Livers were harvested for bulk sequencing at 6, 24, 48, 72, 96 h, 1 week, and 1 month after injection (3 mice per time point), as well as saline injected controls at different time points (2 mice per time point). Livers were dissociated for single-cell sequencing at 24, 48, 72, 96 h, 1 week, and nontreated controls (2–4 mice for each time point, marked with black asterisks). Livers from 24, 48, and 72 h were also taken for Visium spatial transcriptomics (blue asterisks). Mouse injection illustration was created with BioRender.com.

(B) Images of liver lobules at different time points following APAP injection. CV, central vein; PV, portal vein. Yellow dashed lines mark the borders of the damaged areas. Cell nuclei are stained with Dapi (blue). Cell membranes are stained with phalloidin (gray). Scale bars, 20 μ m.

(C) Uniform manifold approximation and projection (UMAP) visualization of the integrated data of all 23,944 cells from 6 time points ($n = 28$ mice). Cells are colored by their cell type annotation.

(D) UMAP visualization of the integrated data. Cells are colored by the time following APAP injection.

See also [Figures S1](#) and [S2](#).

time points after injection. We observed massive pericentral necrosis peaking at 48 h after APAP ([Figure 1B](#)), apparent from the lack of hepatocyte nuclei. The damaged pericentral areas contracted at 72 h with the appearance of new pericentral hepatocytes, which completely replaced the necrotic tissue after 96 h ([Figure 1B](#)). To identify the molecular details of the regeneration process, we performed bulk RNA sequencing (RNA-seq) and single-cell RNA sequencing (scRNA-seq) at multiple time points. In addition, we performed Visium spatial transcriptomics to identify distinct zonal processes during the regeneration process ([Figure 1A](#)). Our bulk RNA-seq included 21 mice sacrificed at 7 time

points after APAP injections, starting at 6 h and up to 1 month following injury (3 mice per time point), and eight controls injected with saline at four different time points ([Table S1](#)). Our scRNA-seq cell atlas included 23,944 cells collected from 28 mice at 6 time points—control, 24, 48, 72, 96 h, and 1 week following injury. The single cells clustered into 11 cell types, each exhibiting distinct marker genes ([Figures 1C, 1D, and S1A](#); [Table S2A](#)). These cell types included hepatocytes, endothelial cells, HSCs, Kupffer cells, cholangiocytes, monocytes, macrophages, plasmacytoid dendritic cells (pDCs), conventional dendritic cells (cDCs), B cells and a cluster of T and NK cells. The Visium dataset

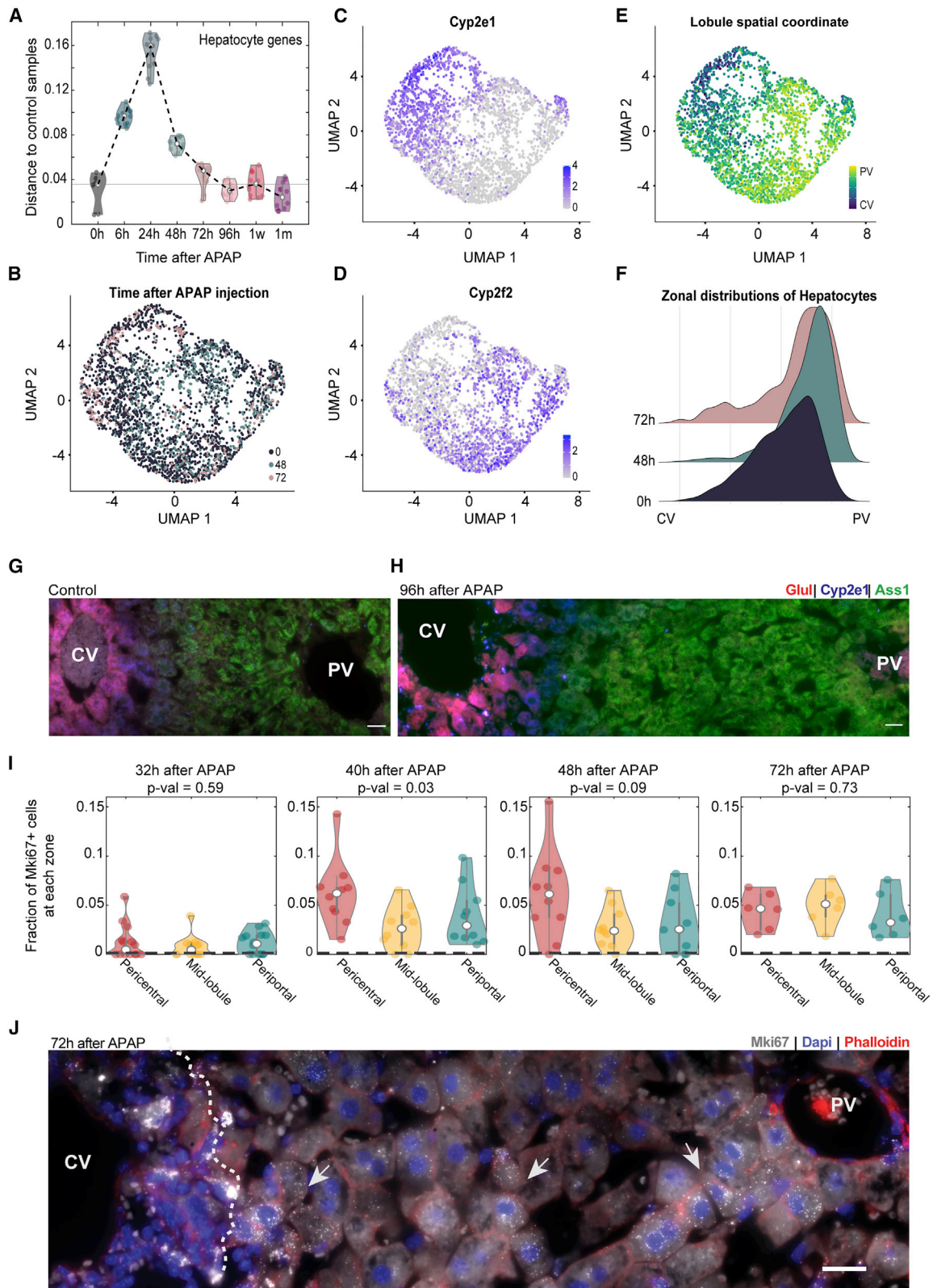


Figure 2. Hepatocytes from all zones proliferate and re-establish zonation

(A) Spearman correlation distances between hepatocyte-specific genes for pairs of control samples ($n = 4$) and mice at different time points ($n = 3$ mice per time point) after APAP injection. Horizontal line denotes median distance of control-control pairs. White dots are median distances for each time point.

(legend continued on next page)

included mice livers taken at 24, 48, and 72 h after APAP injection, two mice from each time point (Figure S2).

Principal component analysis (PCA) of the bulk RNA-seq showed divergence in liver gene expression at 6, 24, and 48 h, with a reversion to the control signature by 96 h (Figure S1B; Table S1). Pathway analysis of the bulk RNA-seq data showed induction of early immune signaling, peaking at 6 and 24 h after APAP. Proliferation pathways peaked at 48 h after APAP (Figure S1C). Liver metabolic functions, such as glutathione and cytochrome P450 metabolism, as well as quiescent HSCs function such as retinol metabolism, were re-emerging at 72 h after APAP.

To quantify the changes in cellular composition of the liver along the course of APAP-induced damage and regeneration, we used computational deconvolution of the bulk data using our scRNA-seq cell-type signatures (Newman et al., 2019) to estimate the relative abundance of each cell type at different time points (STAR Methods; Table S2B). Hepatocyte abundance significantly declined at 48 h after APAP injection, in line with the substantial necrosis of pericentral hepatocytes (Figure 1B), and reverted to the control proportions by 96 h (Figure S1D). In contrast, HSCs, monocytes, and macrophages increased in abundance, peaking at 24–48 h after APAP injection before declining back to control levels (Figure S1D). In accordance with the peak in the abundances of these cell types at 48 h, our scRNA-seq atlas revealed a peak in the proportion of proliferating cells for monocytes, macrophages, and HSCs at 48 h (Figure S1E). Notably, Kupffer cells and endothelial cells also exhibited a peak in proliferation at 48 h, yet did not show a corresponding increase in abundances (Figures S1D and S1E; Table S2B). This could indicate that, in addition to hepatocytes, some Kupffer and endothelial cells may have died during the acute injury phase and have been replenished by proliferation of the remaining cells, as previously demonstrated for Kupffer cells following APAP (Zigmond et al., 2014). Our analysis, therefore, exposes substantial changes in liver gene expression and in proportions of multiple liver cell types, yet a notable rapid reversion to control levels already 4 days after damage. We next set out to characterize the dynamic molecular programs of this regeneration process for distinct liver cell types.

Hepatocytes exhibit zonal reprogramming and broad proliferation across the liver lobule

Pericentral and periportal hepatocytes exhibit distinctly different gene expression in unperturbed livers (Halpern et al., 2017). As observed for the bulk RNA-seq of the complete liver transcriptome (Figures S1B and S1C), the transcriptomes of hepatocyte-specific

genes diverged from controls at early time points but reverted to control levels by 96 h post-APAP injection (STAR Methods; Figure 2A). Our hepatocyte single-cell data consisted of 2,770 cells from control (STAR Methods), 48 and 72 h following APAP injection (Figure 2B). Using the spatial transcriptomics dataset, we identified hepatocyte landmark genes that were either periportal or pericentrally zoned throughout the regeneration process (Figure S2H; Table S3A; Halpern et al., 2018; Moor et al., 2018). We used these to computationally infer the coordinates along the liver lobule axis for the individual sequenced hepatocytes (STAR Methods; Figures 2C–2F). Subsequently, we binned cells from each time point into three zones—pericentral, mid-lobule, and periportal—and averaged their expression to obtain the dynamic hepatocyte zonation profiles (Table S3B). As expected, hepatocytes with a pericentral signature were depleted at 48 h (Figure 2F). The distribution of zonation coordinates approached the preinjury pattern at 72 h (Figure 2F). We used single-molecule fluorescence *in situ* hybridization (smFISH) to demonstrate that classic zoned genes such as the pericentral *Glul* and *Cyp2e1* and the periportal *Ass1* assumed their preinjury zonation patterns at 96 h after damage (Figures 2G, 2H, S3A, and S3B). Notably, although the porto-central distances did not significantly change (Figure S3C), newly formed hepatocytes exhibited significantly higher ploidy levels, an increase that was more prominent in pericentral hepatocytes (Figures S3D and S3E). Our analysis, therefore, shows that hepatocytes reassume their zonal molecular identity 4 days after acute liver damage.

Zonal hepatocyte populations have been shown to exhibit distinct modes of proliferation in homeostasis as well as different regeneration models (He et al., 2021; Sun et al., 2020; Wei et al., 2021). To explore the zonal dynamics of hepatocyte proliferation during APAP regeneration, we analyzed the zonal distributions of proliferating hepatocytes at different time points. To this end, we quantified the fraction of hepatocytes expressing the proliferation marker *Mki67* using smFISH. Hepatocytes proliferated throughout the lobule axis at 32 h after APAP injection, with a slight periportal bias. Proliferation increased at 40 and 48 h, showing a pericentral bias, before leveling off at 72 h (Figures 2I and 2J). Notably, throughout the regeneration process, hepatocytes at the midlobular and portal zones, at large distances from the damaged tissue area, were positive for *Mki67* (Figure 2I and 2J). Differential expression analysis between the proliferating and nonproliferating hepatocytes at distinct lobule zones revealed a decrease in hepatocyte metabolic functions in proliferating hepatocytes (Figure S3F; Table S3C). A similar decrease in hepatocyte metabolic functions in proliferating hepatocytes was recently observed upon deletion

(B) UMAP visualization of hepatocytes ($n = 2,770$ cells), colored by time after APAP injection.

(C) UMAP visualization of hepatocytes colored by the expression of the centrally zoned gene *Cyp2e1*.

(D) UMAP visualization of hepatocytes colored by the expression of the periportal gene *Cyp2f2*.

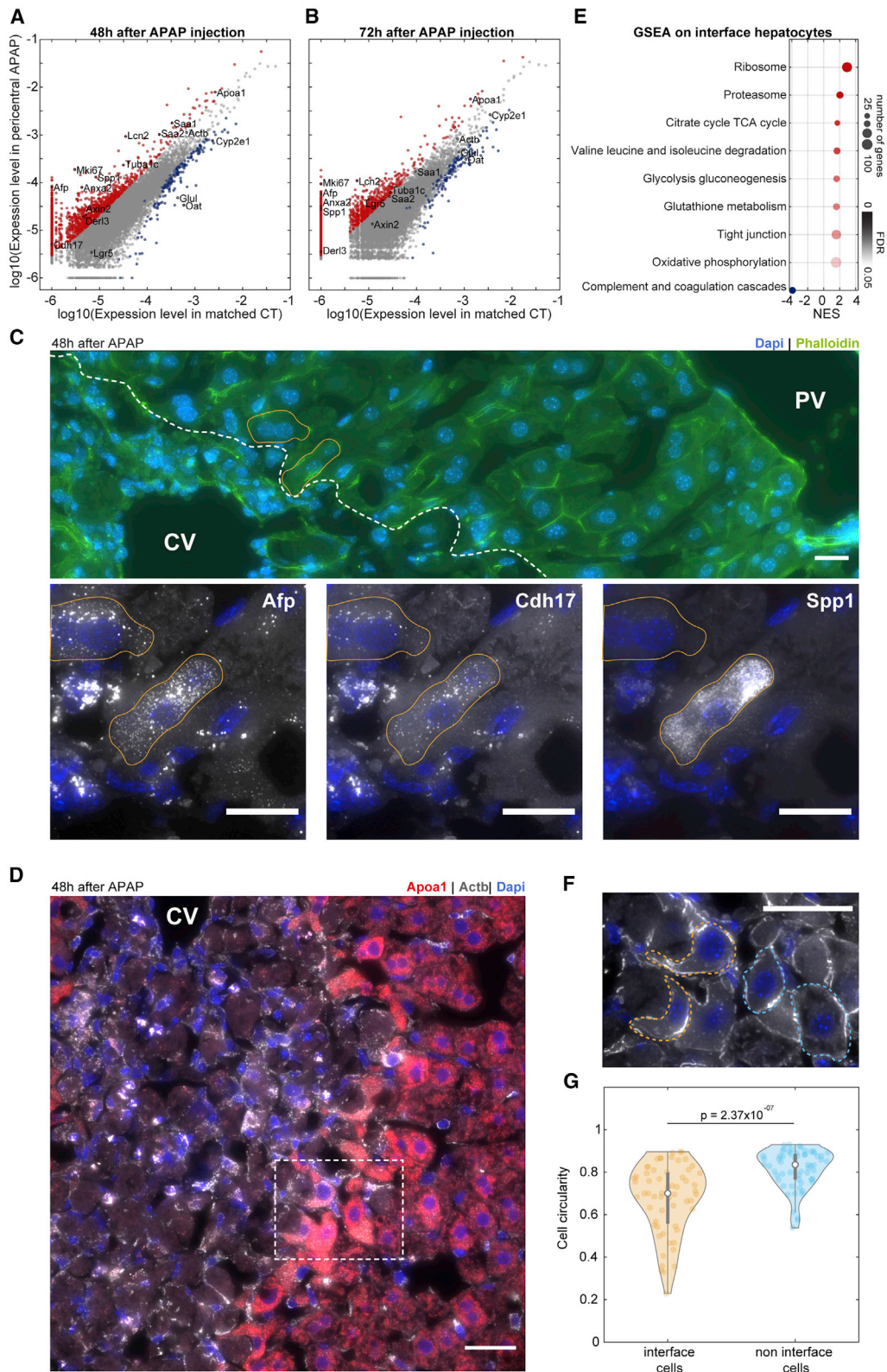
(E) UMAP of hepatocytes colored by their inferred lobule spatial coordinate, ranging from CV—cells closest to central vein, to PV—cells closest to portal vein.

(F) Distributions of lobule spatial coordinates of hepatocytes at each time point.

(G and H) smFISH of a liver lobule showing 3 zoned genes: pericentral *Glul* (red), *Cyp2e1* (blue), and periportal *Ass1* (green). CV, central vein; PV, portal vein. Scale bars, 20 μm . Shown are examples of a control lobule (G) and a lobule 96 h after APAP (H).

(I) The fraction of proliferating hepatocytes expressing *Mki67*+ transcripts out of all hepatocytes located in either pericentral (red), midlobular (yellow), or periportal (green) zones. The analysis was performed on 2 mice from each time point, at least 5 lobules per mouse were quantified. Significance levels calculated using Kruskal-Wallis tests. White dots represent the median fraction.

(J) smFISH of a liver lobule 72 h following APAP administration showing *Mki67* single transcripts (gray dots). Dashed white line marks the damage border, arrows point to representative *Mki67*+ proliferating cells. Cell nuclei are stained with Dapi (blue) and membranes are stained with phalloidin (red). Scale bars, 20 μm . See also Figure S3.



(legend on next page)

of ZNRF3 and RNF43 in hepatocytes (Sun et al., 2021). The broad proliferation of hepatocytes throughout the lobule axis may serve to generate an increased mitotic pressure along the hepatic plates that may contribute to rapidly replacing the cells at the damaged area. Importantly, this mitotic pressure brings midlobular hepatocytes into the pericentral zone, requiring reprogramming their transcriptional states (Figures 2F and 2H).

Interface hepatocytes up-regulate fetal programs and exhibit a mesenchymal shape

To explore the cellular processes involved in the reprogramming of the midlobular hepatocytes into pericentral cell states, we used our scRNA-seq measurements to compare the transcriptomes of the most pericentral hepatocytes at 48 and 72 h and control hepatocytes at corresponding zones (STAR Methods). These hepatocytes constituted the cells at the interface between the damaged and nondamaged zones, which we expected would undergo profound changes in zonal gene expression. We, therefore, termed these cells “interface hepatocytes”. We found that interface hepatocytes exhibited a distinct expression signature, consisting of genes that are expressed in fetal livers and in hepatocellular carcinomas yet not in adult hepatocytes (Figures 3A–3C, S4A, and S4B). These included *Afp*, encoding the fetal serum protein alfa fetoprotein (Camp et al., 2017; Kuhlmann, 1978; Ruoslahti and Seppälä, 1979); *Spp1*, encoding osteopontin (El Makarem et al., 2011; Cabiati et al., 2017; Wang et al., 2016); and *Cdh17*, encoding a cadherin protein associated with activation of Wnt signaling in hepatocellular carcinomas (Bartolomé et al., 2014; Liu et al., 2009; Figure 3C). *Afp* was exclusively expressed by interface hepatocytes and not observed in other lobule layers, yet was expressed by only a subset of interface hepatocytes, indicative of bursty expression (Figures 3C and S5A). Consistent with *Cdh17* expression, interface hepatocytes exhibited elevated levels of Wnt pathway target genes such as *Lgr5* and *Axin2* (Zhao et al., 2019; Figures 3A and 3B). We used smFISH to validate the specific expression of these genes (Figure 3C), as well as of *Apoa1* and *Actb* (Figure 3D) in the hepatocytes residing at the interface between the damaged and nondamaged zones.

Interface hepatocytes upregulated pathways that included ribosomes and proteasomes (Figures 3E and S5B–S5E). These

programs may serve to translate new pericentral proteins, while actively degrading the existing periportal/mid-lobule proteins of these migrating hepatocytes. We found that oxidative phosphorylation was also upregulated in interface hepatocytes, in line with the elevated ATP requirements of active translation (Flamholz et al., 2014). Additionally, pericentral programs such as xenobiotic metabolism (Halpern et al., 2017) were upregulated, whereas periportal programs such as complement and coagulation (Halpern et al., 2017) were downregulated. Interface hepatocytes exhibited a mesenchymal-like shape with elongated extrusions extending into the damage zone (Figures 3D and 3F), with lower circularity compared with non-interface hepatocytes (paired ranksum p value = 2.37×10^{-7} , Figure 3G). These results suggest that interface hepatocytes do not simply switch from a periportal/midlobular state to a pericentral state as they are pushed into the pericentral zone. Rather, their change in cellular identity is associated with a transient expression of fetal genes, elevation of protein translation and degradation, and modified cellular morphology.

HSCs exhibit spatial division of labor

Successful liver regeneration requires tightly coordinated responses from all liver cell types. HSCs are key players in liver damage response and regeneration (Friedman, 2008; Puche et al., 2013). Upon damage sensing, retinol storing quiescent HSCs are activated in a TGF- β -dependent manner and transdifferentiate into collagen-secreting myofibroblasts (Baricos et al., 1999; Tipton and Dabbous, 1998). These activated stellate cells have a central role in extracellular matrix remodeling and fibrosis (Friedman, 2008; Kisseleva and Brenner, 2006; Puche et al., 2013). Previous studies used scRNA-seq to characterize the acute phase of HSC activation (Kolodziejczyk et al., 2020), identifying key cytokines that may be involved in myeloid recruitment. We sought to explore the zonal dynamics of HSCs throughout the regeneration process.

We reclustered the HSC single cells in our atlas and integrated it with a previous scRNA-seq dataset (Kolodziejczyk et al., 2020) of HSCs in control and 20 h post-APAP (STAR Methods; Figure 4A). HSCs have been shown to exhibit zoned gene expression along the lobule axis (Dobie et al., 2019); however, the massive changes in HSC gene expression upon activation may

Figure 3. Interface hepatocytes upregulate onco-fetal genes as they reprogram into pericentral hepatocytes

(A and B) Expression levels of genes in pericentral hepatocytes 48 (A) or 72 h (B) after APAP injection plotted against their expression in control hepatocytes with matched distribution of lobule spatial coordinates. Gray dots represent all genes. Red/blue dots represent genes upregulated/downregulated respectively in the regenerating tissue, with mean expression level of above 5×10^{-6} , at least 2-fold difference from matched control and FDR threshold of 0.01.

(C) smFISH (top) and insets (bottom) of a liver lobule 48 h after APAP injection. Dashed white line delineate the damage border. CV, central vein; PV, portal vein. Nuclei and membranes are labeled with Dapi (blue) and phalloidin (green), respectively. Two representative interface hepatocytes outlined in orange shown in the insets (bottom), together with the smFISH labeling for mRNAs of *Afp* (left), *Cdh17* (middle), and *Spp1* (right). Scale bars, 20 μ m. Laplacian of Gaussian filter was applied on the smFISH images.

(D) smFISH of a liver lobule 48 h post-APAP injection for *Apoa1* (red) and *Actb* (gray) mRNA. Nuclei are stained with Dapi (blue). CV, central vein. Scale bars, 20 μ m. White dashed rectangle is the region displayed in (F).

(E) GSEA normalized enrichment scores (NESs) of gene pathways significantly upregulated (red) or downregulated (blue) in interface cells. Dot size corresponds to number of pathway genes found in the dataset; opacity corresponds to false discovery rate (FDR). Genes sets used for the analysis were taken from Kyoto Encyclopedia of Genes and Genomes (KEGG) pathways dataset.

(F) Magnification of the region marked in (D) showing interface (orange dashed lines) and noninterface (blue dashed lines) hepatocytes. Nuclei and membranes are labeled with Dapi (blue) and phalloidin (gray), respectively. Scale bars, 20 μ m.

(G) Quantification of circularity of interface (orange) and noninterface (blue) hepatocytes. White dots represent group circularity median. Gray boxes mark the 25–75 percentiles. Significance level was calculated using paired signrank test ($n = 60$ pairs of interface and adjacent noninterface hepatocytes, taken from 3 mice 48 h after APAP injection and 3 mice 72 h after APAP injection).

See also Figures S4 and S5.

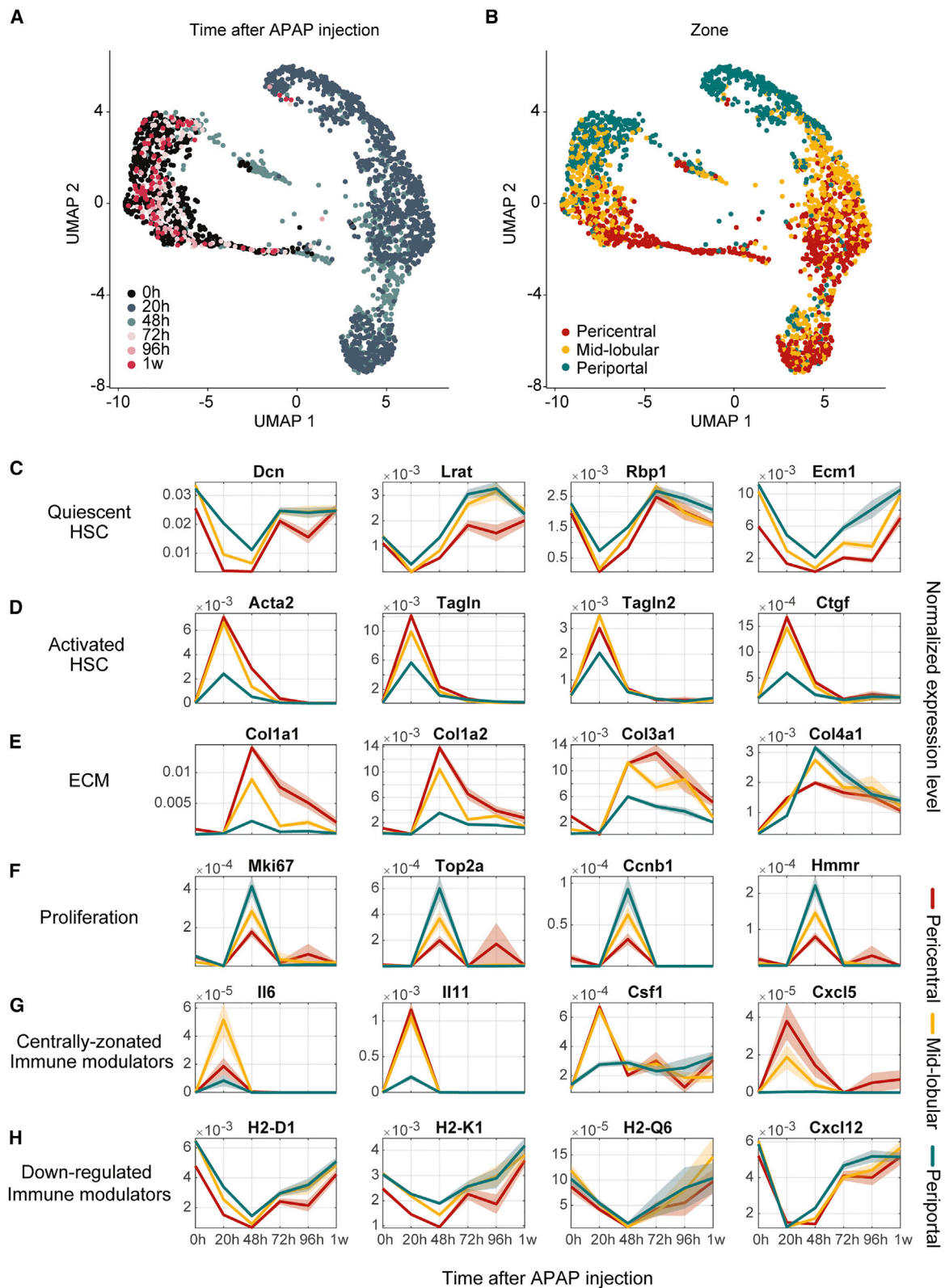


Figure 4. Hepatic stellate cells exhibit distinct expression programs in different zones

(A) UMAP visualization of HSCs, colored by time after APAP administration. $n = 2,311$ cells, at least 2 mice per time point.

(B) UMAP visualization of HSCs, colored by inferred zone (STAR Methods).

(legend continued on next page)

modulate the zonal patterns of HSC landmark genes. To extract zoned HSC landmark genes, we, therefore, used smFISH to validate a periportal abundance of the HSC landmark gene *Ngfr* (Dobie et al., 2019) across all time points (Figures S6A and S6B). We next selected a panel of landmark genes with high single-cell correlations with *Ngfr* at each time point and used these to classify HSCs into pericentral, midlobular, and periportal zones (STAR Methods; Figure 4B). We grouped HSCs from each time and zone to generate spatiotemporally resolved HSC expression profiles (Table S4A). We validated the spatiotemporal dynamics of HSC genes by comparison to our Visium dataset (Figure S2I, $R = 0.65$, $p = 1.7 \times 10^{-40}$).

The levels of quiescent HSC genes such as the retinol binding protein *Rbp1* and lecithin retinol acyltransferase (*Lrat*) declined at all zones and reverted to control levels at 96 h (Figure 4C). Conversely, genes involved in HSC activation, such as the smooth muscle actin gene *Acta2* acutely peaked in expression at 20 h, mainly in pericentral HSCs (Figure 4D). Expression of extracellular matrix (Naba et al., 2016) genes underwent substantial changes along the time course of APAP-induced injury and regeneration in a spatially dependent manner at 48 h most prominently in pericentral HSCs, in line with the required matrix buildup in the damaged zone (Figure 4E and S6C). Notably, the levels of collagen genes remained elevated even at 1 week compared with controls. Similar to collagens, matrix metalloproteinases (MMPs) and metalloproteinase inhibitors (Timp) showed concordant temporal patterns in all zones, peaking in the pericentral zone (Figure S6C).

HSC proliferation genes, which peaked at 48 h, exhibited a higher expression in the periportal and mid-lobule zones compared with the pericentral zone (Figure 4F). Our measurements, therefore, suggest a potential spatial division of labor, whereby pericentral HSCs rapidly respond to the APAP-induced damages, activate and produce ECM, and interact with immune cells, whereas periportal HSCs preferentially proliferate, potentially generating backup HSCs that can migrate into the damaged zone to support the active regeneration process.

In addition to their role in matrix remodeling, HSCs play an important role in the recruitment of myeloid cells into the liver (Pellicoro et al., 2014). Concordant with the pericentrally prevalent fibrogenic processes, immune modulators such *Il6*, *Il11*, the macrophage regulator of proliferation and function, *Csf1* (Chitu and Stanley, 2006), and *Cxcl5* were upregulated primarily in pericentral and mid-lobule HSCs, peaking at 24 h after APAP (Figure 4G). In contrast to the upregulation of myeloid immune modulators, the lymphocyte chemoattractant *Sdf-1*, encoded by the gene *Cxcl12* (Bleul et al., 1996) was strongly downregulated by all HSCs. This is in agreement with the lack of increase in lymphocyte abundance that we have observed throughout the zonal regeneration process (Table S2B). Consistent with this avoidance of lymphocyte activation, HSCs at all zones also exhibited a decline in MHC class 1 genes such as *H2-k1* (Figure 4H).

To identify the molecular pathways of HSC induction, we ran Nichenet (Browaeys et al., 2020), a tool that identifies pathway

activation and highlights potential ligands involved. We found that most of the HSC-activating ligands originated in monocytes and macrophages (e.g., *Gpnmb*), in endothelial cells (e.g., *Tgfa*, *Nid1*), and in HSCs themselves (e.g., *Timp1*, *Ctgf*, Figures S6D and S6E). Our analysis highlights zone-specific HSC expression programs that may facilitate the temporally coordinated processes of immune recruitment, ECM buildup, and breakdown that the liver exhibits following acute APAP damage.

Endothelial cells exhibit zoned cues along the regeneration process

Liver endothelial cells are critical modulators of liver function. They form the building blocks of blood vessels; clear endotoxins, bacteria, and other compounds; regulate host immune responses to pathogens; present antigens; and secrete morphogens that regulate hepatocyte zonal gene expression patterns (Poisson et al., 2017). Importantly, similar to hepatocytes and HSCs, endothelial cells exhibit zoned expression programs (Halpern et al., 2018; Inverso et al., 2021; Xiong et al., 2019). We next asked how zonal endothelial subpopulations support the regeneration process. Our atlas included 6,527 endothelial cells (Figure 5A). Similar to HSCs, we reconstructed endothelial zonation profiles for each of the time points, using distinct set of landmark genes for each time point (STAR Methods; Table S4B). Examples for zoned genes include the pericentral *Wnt2* and the periportal *Efnb2* (Halpern et al., 2018; Figure 5B), as well as markers for sinusoidal endothelial cells (*Kit*; Halpern et al., 2018) and vascular endothelial cells (*Vwf*; Kalucka et al., 2020) to classify the endothelial cells into 5 zonal population (STAR Methods). These included pericentral liver vascular endothelial cells (PC-LVECs); pericentral, midlobular, and periportal liver sinusoidal endothelial cells (PC-LSECs, mid-LSECs, and PP-LSECs); and periportal liver vascular endothelial cells (PP-LVECs, Figure 5C; STAR Methods). As with hepatocytes and HSCs, we validated the zonation patterns of endothelial cells by comparisons with our Visium dataset (Figure S2J; $R = 0.63$, $p = 5.5 \times 10^{-24}$).

Pericentral vascular endothelial cells, a major source of the morphogens *Wnt2*, *Wnt9b*, and *Rspo3* that establish many of the hepatocyte pericentral programs (Benhamouche et al., 2006; Mak and Png, 2020; Monga, 2015; Planas-Paz et al., 2016), showed a transient decline in the expression of these morphogens at 24 h and an ensuing slight overshoot (Figures 5D and S6F–S6H). *Wnt9b*, which was shown to be implicated in liver regeneration after partial hepatectomy (Preziosi et al., 2018), was transiently downregulated 48 h after APAP injection in PC-LVEC. Importantly, expression of these Wnt ligands seemed to precede the reappearance of pericentral hepatocyte gene expression (Figure S6I).

PC-LVEC also exhibited a decline in MHC class 1 and MHC class 2 molecules. This is in line with the decline we observed in HSC MHC-I expression (Figure 4G) and could serve to avoid unwanted lymphocyte activation by the presentation of antigens

(C–H) Temporal dynamics of selected genes in HSCs, stratified by zone. Lines denote the mean of the normalized expression over cells from the same zone and time point, patches denote the standard errors of the means (SE). For each gene, the mean and SE for pericentral HSCs (red), mid-lobule HSCs (yellow) and periportal HSCs (green) are presented. Selected genes belong to various processes: markers of quiescent HSCs (C), activated HSCs (D), ECM collagen genes (E), proliferation (F), centrally zoned immune modulators (G), and downregulated zoned immune modulators (H). See also Figure S6.

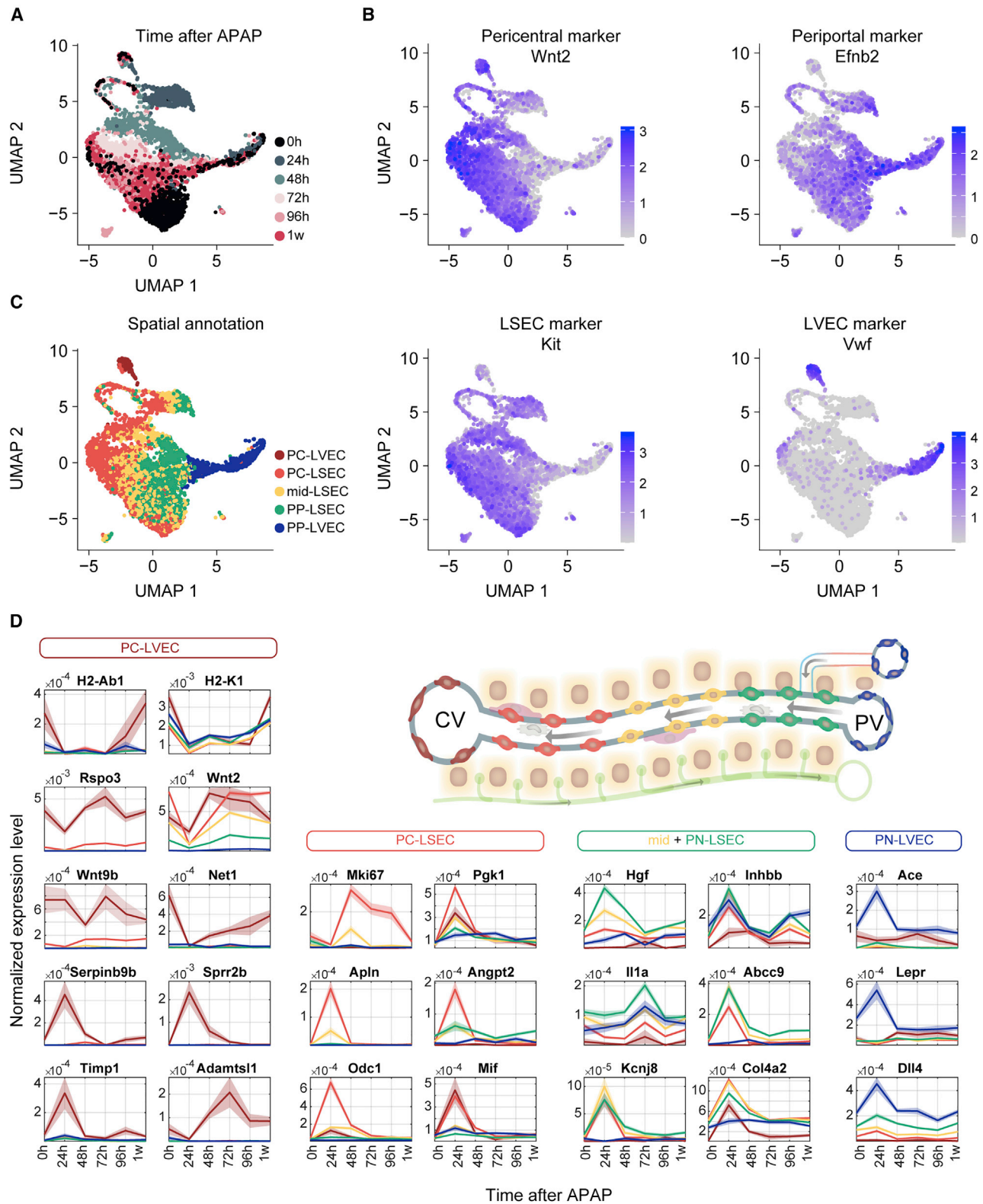


Figure 5. Zonal endothelial cell populations differentially express genes involved in the regeneration process

(A) UMAP visualization of endothelial cells, colored by time after APAP administration. n = 6,527 from 13 mice, at least 2 mice per time point.

(B) UMAP visualization of endothelial cells, colored by expression level of the pericentral *Wnt2* (top left), periportal *Efnb2* (top right), sinusoidal endothelial cell marker *Kit* (bottom left) and vascular endothelial cell marker *Vwf* (bottom right).

(legend continued on next page)

scavenged from necrotic hepatocytes. PC-LVEC expressed the metalloproteinase inhibitor *Timp1* at 24 h and the metalloproteinase *Adamts1* at 72 h, consistent with the need to counteract ECM breakdown at the initial stages of regeneration and apply ECM breakdown during resolution. Pericentral and midlobular sinusoidal endothelial cells showed the most notable upregulation of proliferation genes such as *Mki67* (Figure 5D). This could indicate that in addition to hepatocytes, PC-LSECs at the damage zone are also dying and replaced by proliferation of remaining neighboring cells. *Hgf*, a major mitogen for hepatocytes (Nakamura et al., 1984), was broadly expressed by sinusoidal, yet not by vascular endothelial cells, with a slight periportal zonation bias (Figure 5D). This broad expression could account for the broad pattern of hepatocyte proliferation we have observed (Figures 2I and 2J). This finding further supports the notion that hepatocyte proliferation and differentiation are uncoupled after APAP damage. Although *Hgf* was broadly expressed, Wnt morphogens were expressed in the pericentral zones, potentially serving to induce pericentral hepatocyte programs in newly incoming regenerating hepatocytes (Figure S6I).

To identify potential transcription factors that may be associated with the induction of *Hgf* expression in both endothelial cells and HSCs, we performed gene regulatory network analysis using the Single-cell regulatory network inference and clustering (SCENIC) tool (Aibar et al., 2017; Van de Sande et al., 2020). Upstream transcription factors associated with *Hgf* activation that showed significant elevation in activity in the *Hgf*+ cells included *Ets1* (Dittmer, 2003), *Ets2*, *Hlx* (Hentsch et al., 1996), and *Tead1* (Corley et al., 2018; Table S4C).

Dynamics of myeloid cell subtypes along the regeneration process

Myeloid cells are instrumental to the regeneration process following acute liver damage (Goldin et al., 1996; Kolodziejczyk et al., 2020; Tacke and Zimmermann, 2014). Our atlas included 9,338 myeloid cells, clustered into 10 cell types with distinct marker (Figures 6A–6C and S7A). Monocytes peaked in proportion at 24 h, whereas macrophages peaked at 48 h, potentially indicating maturation from incoming monocytes, as previously shown in the liver after damage (Karlmark et al., 2009; Zigmond et al., 2014). Kupffer cells exhibited a distinct activated cell state at 24 and 48 h, yet returned to their control states by 96 h (Figures 6A–6C). Importantly, Kupffer cells and monocytes formed distinct clusters at all time points (Ginhoux and Guillems, 2016). This is consistent with the previous observation that dying Kupffer cells are replaced via proliferation of surviving Kupffer cells, rather than from incoming monocytes after acute liver damage (Zigmond et al., 2014). Activated Kupffer cells showed both distinct and shared programs with macrophages (Figures S7B–S7D). Kupffer cells showed elevated interferon

alpha and gamma responses, whereas macrophages exhibited elevated KRAS, IL2, STAT5, MYC, and mTOR signaling (Figure S7E).

As with HSCs and endothelial cells, both Kupffer cells and macrophages exhibited a drop in expression of genes encoding the antigen presentation machinery, such as *Cd74* and *H2-Q4* (Figure S7F). Consistently, lymphocyte-attracting chemokines, such as *Cxcl9*, *Cxcl10*, and *Cxcl13*, were also downregulated (Figure S7F). Additional shared programs included upregulation of chemokines, such as *Ccl2*, *Ccl7*, and *Ccl9*. Kupffer cells also exhibited higher expressions of proliferation markers, such as *Mki67*, *Pcna*, and *Top2a* (Figures S7C, S7D, and S7F), suggesting that Kupffer cells are proliferating more than the recruited macrophages in the liver during regeneration.

The most upregulated gene in activated Kupffer cells was *Mmp12*, encoding for the elastase matrix metalloproteinase 12 enzyme (Belaouaj et al., 1995; Werb and Gordon, 1975). *Mmp12* expression levels were 637-fold higher at 24 h compared with controls (Kruskal-Wallis p ($df_5, 2,838$) = 3.37×10^{-127} , Table S2). *Mmp12* also exhibited upregulation in macrophages (Figure 6D). Notably, when imaging the expression of *Mmp12* using smFISH, we found it to be expressed in myeloid cells localized at the damage zone (Figure 6E). Both *Mmp12*+ Kupffer cells and *Mmp12*+ macrophages upregulated genes found in lipid-associated macrophages (Jaitin et al., 2019; Remmerie et al., 2020), such as *Trem2*, *Lpl*, and *Cd36* (Figure S7F). Expression of these genes was higher in macrophages (Figures S7D and S7F).

As with hepatocytes and endothelial cells, activated Kupffer cell showed significant correlation with fetal Kupffer cells (Figures S4E and S4F, $R = 0.59$, $p < 1 \times 10^{-40}$). Common trends with fetal Kupffer cells included the reduction in antigen presentation genes and an increase in lipid-associated macrophage genes (Figure S4E).

DISCUSSION

Liver zonal regeneration is a remarkable process achieved rapidly and precisely by the coordinated action of multiple cell types. These cell types exhibit both zone-independent and zone-specific gene expression programs (Figure 7). Hepatocyte proliferation occurs throughout the lobule axis, presumably to generate a large mitotic pressure. In turn, this pressure pushes the neighboring hepatocytes to repopulate the damaged zone, as has been previously shown for both periportal and pericentral models of liver injury (Sun et al., 2020). This broad proliferation could be induced by hepatocyte growth factor, which we found to be expressed by HSCs and sinusoidal endothelial cells at all zones, rather than exclusively at the pericentral damaged zone. We found that the incoming mid-lobular hepatocytes do not

(C) UMAP visualization of endothelial cells, colored by inferred zone (STAR Methods). PC-LVECs, pericentral liver vascular endothelial cells; PC-LSECs, pericentral liver sinusoidal endothelial cells; mid-LSECs, mid-lobule liver sinusoidal endothelial cells; PP-LSECs, periportal liver sinusoidal endothelial cells; PP-LVECs, periportal liver vascular endothelial cells.

(D) Temporal dynamics of selected genes in endothelial cells, stratified by the zoned endothelial cell populations. Lines denote the mean of the normalized expression over cells from the same zone and time point, patches denote the standard errors of the means (SE). For each gene, the mean and SE for PC-LVEC (dark red), PC-LSEC (red), mid-LSEC (yellow), PP-LSEC (green), and PP-LVEC (blue) are presented. Lobule diagram highlights the different zoned endothelial cell subtypes with their respective colors.

See also Figures S4 and S6.

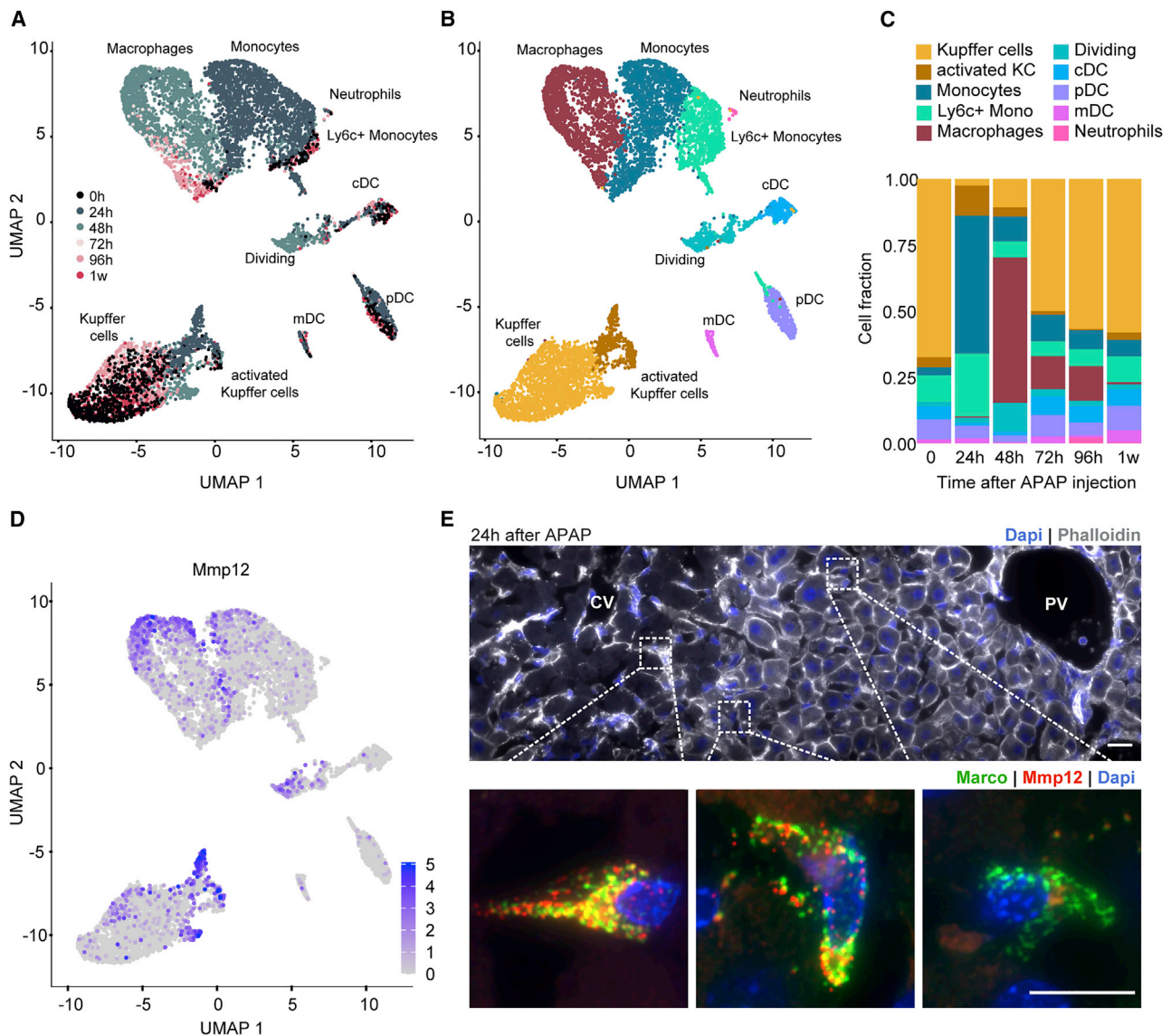


Figure 6. Spatiotemporal patterns of myeloid cell gene expression

(A) UMAP visualization of myeloid cell populations, colored by time after APAP administration. $n = 9,338$ cells from 15 mice, at least 2 mice per time point.

(B) UMAP visualization of myeloid cell populations, colored by cell types.

(C) The fractions of different myeloid cell subtypes at each time point.

(D) UMAP visualization of myeloid cells, colored by expression levels of *Mmp12*.

(E) smFISH scan (top) and zoomed-in insets (bottom) of a liver lobule 24 h after APAP injection. CV, central vein; PV, portal vein. Nuclei and membranes are labeled with Dapi (blue) and phalloidin (green), respectively. Pericentral (left), mid-lobule (middle), and periportal (right) KCs marked by dashed lines in the scan are enlarged in the insets (bottom), together with the smFISH for the Kupffer cell gene *Marco* (green) and *Mmp12* (red) mRNAs, together with Dapi (blue). Scale bars, 20 μm for top image, 10 μm for insets. Laplacian of Gaussian filter was applied on the smFISH images.

See also [Figures S4](#) and [S7](#).

directly trans-differentiate into pericentral hepatocytes. Rather, interface hepatocytes that are pushed pericentrally to seal the damaged zone exhibit a distinct gene expression signature observed in fetal yet not in adult livers. This signature includes genes such as *Afp*, *Cdh17* and *Spp1*, which are normally expressed in the fetal liver or in hepato-cellular carcinoma. This finding, together with the higher correlation of pericentral LSECs and KCs at 24h after APAP injection with their fetal counterparts, resemble the onco-fetal microenvironment observed in

hepatocellular carcinoma ([Sharma et al., 2020](#)). This may imply an overall reprogramming mechanism in the liver. *Afp* has been shown to be expressed at the margins of necrotic tissues following CCl_4 intoxication ([Iwai et al., 2000](#)), as well as around fibrotic bridges in chronic liver damage ([Nakano et al., 2017](#)). Moreover, serum levels of the AFP protein following acute APAP damage correlate with survival ([Schjødt et al., 2006](#); [Schmidt and Dalhoff, 2005](#); [Singh et al., 2019](#)), consistent with our detected robust expression in reprogramming zonal

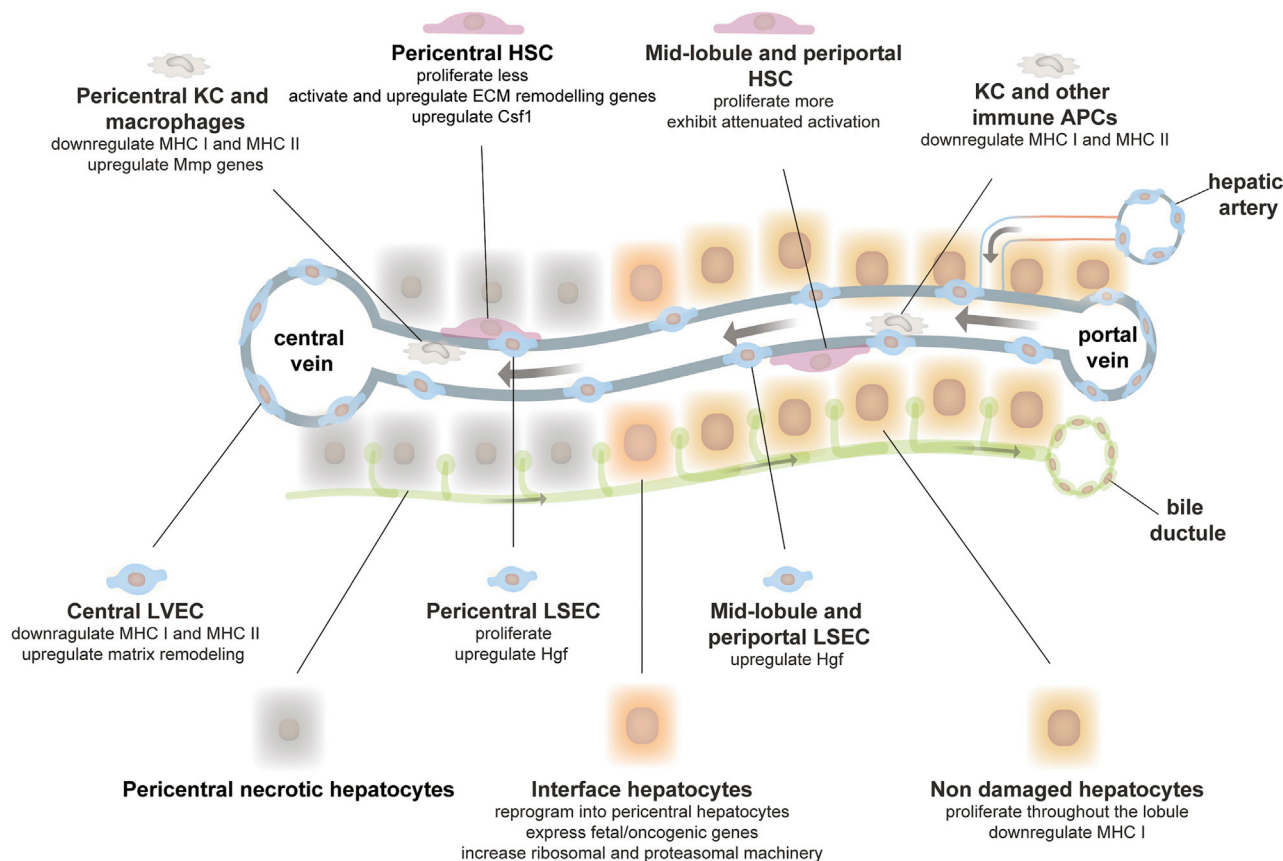


Figure 7. Summary of main events during APAP-induced liver damage and regeneration

A commented illustration of a liver lobule summarizing the main zone-dependent and independent changes in the different liver cell types during the regeneration process.

hepatocytes. We found that interface hepatocytes have a distinct non-circular morphology and elevated levels of ribosomes and proteasomes. This elevation of the protein turnover machinery could serve to facilitate the required rapid turnover of their proteome, as periportal proteins need to be eliminated and pericentral proteins formed. The fact that hepatocytes were proliferating throughout the lobule, coupled with the distinctly different zonal patterns of the pericentral Wnt morphogens and the broad Hgf mitogens, suggest that the processes of cell division and reprogramming may be uncoupled during zonal liver regeneration. The logic of this is that reprogramming needs to be performed mainly in the damaged zone, while broad proliferation serves to seal the damage rapidly through elevated mitotic pressure. Regeneration following zonal damage has been shown to be delayed in a mouse model with Wnt/beta-catenin inhibition (Apte et al., 2009). It would be interesting to apply our spatiotemporal approach to study the changes in the regeneration programs upon *Wnt* or *Hgf* inhibition, to gain insight into the molecular interplay of these important signals and their role in liver regeneration and proliferation (Apte et al., 2006). Furthermore, it would be important to identify the cues that give rise to the fetal reprogramming of interface hepatocytes, be they mechanosensing of the contact with the fibrotic zones or distinct morphogens.

Although zonal regeneration involved the massive transient recruitment of monocytes and macrophages, lymphocyte abundance showed stability in cell numbers (Table S2B). The avoidance of induction of adaptive immunity may be critical, given the multiple new antigens available for presentation due to the necrotic hepatocytes. Indeed, we found that all cell types transiently reduced the expression of MHC-I genes and that the liver antigen presenting cells—endothelial cells and myeloid cells transiently reduced MHC-II genes up to 96 h after damage. The induction in myeloid-recruiting cytokines, such as *Ccl2*, *Ccl7*, and *Csf1*, and the repression of signals for recruitment of lymphocytes, such as *Cxcl12* and *Cxcl13*, may also contribute to the inverse abundances of myeloid and lymphocyte populations.

Our study exposed intricate zone-dependent expression programs of HSCs and endothelial cells. We found that pericentral HSCs massively induced ECM programs, such as collagen gene expression, whereas periportal HSCs showed increased proliferation. Response to zonal damage requires massive matrix remodeling. To achieve this, the liver needs to generate new HSCs and to activate them to achieve maximal secretion of matrix components as fast as possible. Both HSC proliferation and the production of secreted matrix proteins require cellular resources that may be limited. Our analyses suggest a strategy

of spatial resource allocation, whereby pericentral HSCs are early responders that initiate matrix production immediately, whereas portal HSCs divide to provide backup cells that can later migrate into the damaged zone and reduce the load from the pericentral HSCs. Our study also provides the molecular details of the resolution of the fibrogenesis involved in zonal regeneration. These could prove informative for the goals of resolving fibrotic states (Adler et al., 2020; Henderson and Iredale, 2007; Kisseleva and Brenner, 2006; Liu et al., 2020; Puche et al., 2013; Troeger et al., 2012). Our analysis also revealed zoned proliferation patterns of endothelial cells, which were restricted to pericentral and midlobular sinusoidal endothelial cells but not pericentral vascular endothelial cells. These vascular endothelial cells, which form the central blood vessels and are nonfenestrated, might be more robust to the toxic microenvironment generated following hepatocyte necrosis and myeloid cell migration. In summary, our work highlighted the details of liver plasticity during zonal regeneration and exposed the zone-dependent coordinated programs that facilitate precise healing of the liver tissue.

Limitations of the study

The RNA-seq and imaging approaches implemented in this study provide high-resolution measurements of the spatial and dynamics of liver transcriptome along the liver damage and regeneration processes. Nevertheless, post-transcriptional regulation as well as sequestering and exposing of molecules by the vastly changing ECM are hard to detect directly in our datasets. Examples of such regulation levels are PDGF, TGF- β , and HGF (Hynes, 2009). Moreover, the short time frame of 4 days at which the complete zonal regeneration process is attained is within the order of magnitude of typical protein lifetimes (Schwanhäusser et al., 2011). In such out-of-steady-state regime, a complete functional view of the regeneration process will require analysis of proteins. It will, therefore, be informative to apply approaches such as spatial sorting (Ben-Moshe et al., 2019; Harnik et al., 2021; Inverso et al., 2021) to assess the dynamics of liver proteome in a cell- and zone-specific manner. Our study focused on pericentral zonal damage. It will be interesting to use similar methods to explore whether interface hepatocytes, immune evasion, and matrix remodeling also apply to periportal damage (Ben-Moshe and Itzkovitz, 2019).

In this study, liver damage and regeneration were sampled every 24 h. Although this time window captures the phases of damage and regeneration, there might be processes that would be fully characterized by higher temporal resolution.

STAR★METHODS

Detailed methods are provided in the online version of this paper and include the following:

- KEY RESOURCES TABLE
- RESOURCE AVAILABILITY
 - Lead contact
 - Materials availability
 - Data and code availability
- EXPERIMENTAL MODEL AND SUBJECT DETAILS
- METHODS DETAILS

- Single molecule fluorescence in-situ hybridization (smFISH)
- Library construction for bulk liver mRNA
- Data processing for bulk mRNA
- Principal component analysis on bulk samples
- Liver perfusions and hepatocyte dissociation
- Liver perfusions of non-parenchymal cell (NPC)
- TotalSeq™-B for 10x feature barcoding
- Single cell libraries with feature barcoding
- Single-cell RNAseq data analysis
- Data pre-processing and background subtraction
- Data processing of NPCs using Seurat package
- Data integration of NPCs
- Hepatocyte processing
- Data integration of hepatocytes
- Finding markers for different cell types
- Estimating cellular composition using CIBERSORTx
- Temporal dynamics of KEGG pathways
- Extracting hepatocyte temporal changes
- Visium 10x spatial transcriptomics
- Spatial transcriptomics processing
- Inferring lobule spatial coordinates of single hepatocytes
- Analyzing proliferation in hepatocytes
- Comparing proliferating and non-proliferating hepatocytes
- Comparing interface hepatocytes and control
- Gene Set Enrichment Analysis (GSEA) of interface hepatocytes
- Measuring length of porto-central axes
- Measuring nucleus diameter of hepatocytes
- Hepatic stellate cell cluster analysis
- Inferring lobule spatial coordinates of single HSCs
- Spatio-temporal analysis of the matrisome
- Ligand-target interaction analysis of activated HSC
- Endothelial cell cluster analysis
- Inferring lobule spatial coordinates of single endothelial cells
- Validations of spatial reconstruction using spatial transcriptomics dataset
- Identifying putative transcription factors upstream of Hgf
- Myeloid clusters analysis
- GSEA of activated Kupffer cells and macrophages
- Interaction analysis from scRNAseq dataset
- Interaction analysis from spatial transcriptomics dataset
- Comparing regenerating cells with fetal datasets
- QUANTIFICATION AND STATISTICAL ANALYSIS
- ADDITIONAL RESOURCES

SUPPLEMENTAL INFORMATION

Supplemental information can be found online at <https://doi.org/10.1016/j.stem.2022.04.008>.

ACKNOWLEDGMENTS

S.I. was supported by the Helen and Martin Kimmel Institute for Stem Cell Research, the Wolfson Family Charitable Trust, the Edmond de Rothschild

Foundations, the Fannie Sherr Fund, the Dr. Beth Rom-Rymer Stem Cell Research Fund, the Minerva Stiftung grant, the Israel Science Foundation grant no. 1486/16, the Broad Institute-Israel Science Foundation grant no. 2615/18, the European Research Council (ERC) under the European Union's Horizon 2020 research and innovation program grant no. 768956, the Chan Zuckerberg Initiative grant no. CZF2019-002434, the Bert L. and N. Kuggie Vallee Foundation, and the Howard Hughes Medical Institute (HHMI) international research scholar award. We would like to thank Ehud Zigmund from Tel Aviv Sourasky Medical Center for fruitful discussions and Merav Kedmi, Orit Zion, and Hadas Keren-Shaul from Weizmann Institute Life Sciences Core Facilities for their assistance in sequencing.

AUTHOR CONTRIBUTIONS

S.I., K.B.H., and S.B.-M. conceived the study. S.B.-M. designed and performed the scRNA-seq experiments. T.V. and S.B.-M. performed the bulk liver mRNA-seq experiment. K.B.H. performed the Visium spatial transcriptomics experiments. S.B.-M., K.B.H., T.V., S.D., and R.M. performed the smFISH experiments. S.B.-M. and S.I. performed data analysis. D.P. quantified the liver lobule sizes. A.A.K. and E.E. assisted with obtaining HSC data. A.L. constructed the web browser. S.I. and S.B.-M. wrote the manuscript. S.I. supervised the study. All authors discussed the results and commented on the manuscript.

DECLARATION OF INTERESTS

The authors declare no competing interests.

Received: September 3, 2021

Revised: February 28, 2022

Accepted: April 12, 2022

Published: June 2, 2022

REFERENCES

- Achim, K., Pettit, J.-B., Saraiva, L.R., Gavriouchkina, D., Larsson, T., Arendt, D., and Marioni, J.C. (2015). High-throughput spatial mapping of single-cell RNA-seq data to tissue of origin. *Nature Biotechnology* 33, 503–509. <https://doi.org/10.1038/nbt.3209>.
- Adler, M., Mayo, A., Zhou, X., Franklin, R.A., Meizlish, M.L., Medzhitov, R., Kallenberger, S.M., and Alon, U. (2020). Principles of cell circuits for tissue repair and fibrosis. *iScience* 23, 100841. <https://doi.org/10.1016/j.isci.2020.100841>.
- Aibar, S., González-Blas, C.B., Moerman, T., Huynh-Thu, V.A., Imrichova, H., Hulselmans, G., Rambow, F., Marine, J.-C., Geurts, P., Aerts, J., et al. (2017). SCENIC: single-cell regulatory network inference and clustering. *Nat. Methods* 14, 1083–1086. <https://doi.org/10.1038/nmeth.4463>.
- Apte, U., Singh, S., Zeng, G., Cieply, B., Virji, M.A., Wu, T., and Monga, S.P.S. (2009). Beta-catenin activation promotes liver regeneration after acetaminophen-induced injury. *Am. J. Pathol.* 175, 1056–1065. <https://doi.org/10.2353/ajpath.2009.080976>.
- Apte, U., Zeng, G., Muller, P., Tan, X., Micsenyi, A., Cieply, B., Dai, C., Liu, Y., Kaestner, K.H., and Monga, S.P.S. (2006). Activation of Wnt/ β -catenin pathway during hepatocyte growth factor-induced hepatomegaly in mice. *Hepatology* 44, 992–1002. <https://doi.org/10.1002/hep.21317>.
- Bagnoli, J.W., Ziegenhain, C., Janjic, A., Wange, L.E., Vieth, B., Parekh, S., Geuder, J., Hellmann, I., and Enard, W. (2018). Sensitive and powerful single-cell RNA sequencing using mcSCR-seq. *Nature Communications* 9, 2937. <https://doi.org/10.1038/s41467-018-05347-6>.
- Baricos, W.H., Cortez, S.L., Deboisblanc, M., and Xin, S. (1999). Transforming growth factor- β is a potential inhibitor of extracellular matrix degradation by cultured human mesangial cells. *J. Am. Soc. Nephrol.* 10, 790–795. <https://doi.org/10.1681/ASN.V104790>.
- Bartolomé, R.A., Barderas, R., Torres, S., Fernandez-Aceñero, M.J., Mendes, M., García-Foncillas, J., Lopez-Lucendo, M., and Casal, J.I. (2014). Cadherin-17 interacts with α 2 β 1 integrin to regulate cell proliferation and adhesion in colorectal cancer cells causing liver metastasis. *Oncogene* 33, 1658–1669. <https://doi.org/10.1038/onc.2013.117>.
- Belaouaj, A., Shipley, J.M., Kobayashi, D.K., Zimonjic, D.B., Popescu, N., Silverman, G.A., and Shapiro, S.D. (1995). Human macrophage metalloelastase. Genomic organization, chromosomal location, gene linkage and tissue-specific expression *. *J. Biol. Chem.* 270, 14568–14575. <https://doi.org/10.1074/jbc.270.24.14568>.
- Benhamouche, S., Decaens, T., Godard, C., Chambrey, R., Rickman, D.S., Moinard, C., Vasseur-Cognet, M., Kuo, C.J., Kahn, A., Perret, C., and Colnot, S. (2006). Apc tumor suppressor gene is the “zonation-keeper” of mouse liver. *Dev. Cell* 10, 759–770. <https://doi.org/10.1016/j.devcel.2006.03.015>.
- Ben-Moshe, S., and Itzkovitz, S. (2019). Spatial heterogeneity in the mammalian liver. *Nat. Rev. Gastroenterol. Hepatol.* 16, 395–410. <https://doi.org/10.1038/s41575-019-0134-x>.
- Ben-Moshe, S., Shapira, Y., Moor, A.E., Manco, R., Veg, T., Bahar Halpern, K., and Itzkovitz, S. (2019). Spatial sorting enables comprehensive characterization of liver zonation. *Nat. Metab.* 1, 899–911. <https://doi.org/10.1038/s42255-019-0109-9>.
- Bhushan, B., and Apte, U. (2019). Liver regeneration after acetaminophen hepatotoxicity: mechanisms and therapeutic opportunities. *Am. J. Pathol.* 189, 719–729. <https://doi.org/10.1016/j.ajpath.2018.12.006>.
- Bleul, C.C., Fuhlbrigge, R.C., Casanovas, J.M., Aiuti, A., and Springer, T.A. (1996). A highly efficacious lymphocyte chemoattractant, stromal cell-derived factor 1 (SDF-1). *J. Exp. Med.* 184, 1101–1109. <https://doi.org/10.1084/jem.184.3.1101>.
- Browaeys, R., Saelens, W., and Saeyns, Y. (2020). NicheNet: modeling intercellular communication by linking ligands to target genes. *Nat. Methods* 17, 159–162. <https://doi.org/10.1038/s41592-019-0667-5>.
- Butler, A., Hoffman, P., Smibert, P., Papalexi, E., and Satija, R. (2018). Integrating single-cell transcriptomic data across different conditions, technologies, and species. *Nature Biotechnology* 36, 411–420. <https://doi.org/10.1038/nbt.4096>.
- Cabiati, M., Gaggini, M., Cesare, M.M., Caselli, C., De Simone, P., Filipponi, F., Basta, G., Gastaldelli, A., and Del Ry, S. (2017). Osteopontin in hepatocellular carcinoma: a possible biomarker for diagnosis and follow-up. *Cytokine* 99, 59–65. <https://doi.org/10.1016/j.cyto.2017.07.004>.
- Camp, J.G., Sekine, K., Gerber, T., Loeffler-Wirth, H., Binder, H., Gac, M., Kanton, S., Kageyama, J., Damm, G., Seehofer, D., et al. (2017). Multilineage communication regulates human liver bud development from pluripotency. *Nature* 546, 533–538. <https://doi.org/10.1038/nature22796>.
- Chitu, V., and Stanley, E.R. (2006). Colony-stimulating factor-1 in immunity and inflammation. *Curr. Opin. Immunol.* 18, 39–48. <https://doi.org/10.1016/j.coi.2005.11.006>.
- Corley, S.M., Mendoza-Reinoso, V., Giles, N., Singer, E.S., Common, J.E., Wilkins, M.R., and Beverdam, A. (2018). Plau and Tgfb β 3 are YAP-regulated genes that promote keratinocyte proliferation. *Cell Death Dis* 9, 1106. <https://doi.org/10.1038/s41419-018-1141-5>.
- Deczkowska, A., David, E., Ramadori, P., Pfister, D., Safran, M., At The, B., Giladi, A., Jaitin, D.A., Barbov, O., Cohen, M., Yofe, I., Gur, C., Shlomi-Loubaton, S., Henri, S., Suhail, Y., Qiu, M., Kam, S., Hermon, H., Lahat, E., and Amit, I. (2021). XCR1+ type 1 conventional dendritic cells drive liver pathology in non-alcoholic steatohepatitis. *Nature Medicine* 27, 1043–1054. <https://doi.org/10.1038/s41591-021-01344-3>.
- Devroye, L. (2006). Chapter 4. Nonuniform random variate generation. In *Handbooks in Operations Research and Management Science*, 13, S.G. Henderson and B.L. Nelson, eds. (Elsevier), pp. 83–121. [https://doi.org/10.1016/S0927-0507\(06\)13004-2](https://doi.org/10.1016/S0927-0507(06)13004-2).
- Dittmer, J. (2003). The biology of the Ets1 proto-oncogene. *Mol. Cancer* 2, 29. <https://doi.org/10.1186/1476-4598-2-29>.
- Dobie, R., Wilson-Kanamori, J.R., Henderson, B.E.P., Smith, J.R., Matchett, K.P., Portman, J.R., Wallenborg, K., Picelli, S., Zagorska, A., Pendem, S.V., et al. (2019). Single-cell transcriptomics uncovers zonation of function in the

- mesenchyme during liver fibrosis. *Cell Rep.* 29, 1832–1847.e8. <https://doi.org/10.1016/j.celrep.2019.10.024>.
- Drain, C., Kholtei, J.E., Bahar Halpern, K., Hurni, C., Rozenberg, M., Muvkadi, S., Itzkovitz, S., and Naef, F. (2021). Space-time logic of liver gene expression at sub-lobular scale. *Nature Metabolism* 3, 43–58. <https://doi.org/10.1038/s42255-020-00323-1>.
- El Makarem, M.A.A., Abdel-Aleem, A., Ali, A., Saber, R., Shatat, M., Rahem, D.A., and Sayed, D. (2011). Diagnostic significance of plasma osteopontin in hepatitis C virus-related hepatocellular carcinoma. *Ann. Hepatol.* 10, 296–305. [https://doi.org/10.1016/S1665-2681\(19\)31541-8](https://doi.org/10.1016/S1665-2681(19)31541-8).
- Flamholz, A., Phillips, R., and Milo, R. (2014). The quantified cell. *Mol. Biol. Cell* 25, 3497–3500. <https://doi.org/10.1091/mbc.E14-09-1347>.
- Friedman, S.L. (2008). Hepatic stellate cells: protean, multifunctional, and enigmatic cells of the liver. *Physiol. Rev.* 88, 125–172. <https://doi.org/10.1152/physrev.00013.2007>.
- Gebhardt, R. (1992). Metabolic zonation of the liver: regulation and implications for liver function. *Pharmacol. Ther.* 53, 275–354. [https://doi.org/10.1016/0163-7258\(92\)90055-5](https://doi.org/10.1016/0163-7258(92)90055-5).
- Ginhoux, F., and Williams, M. (2016). Tissue-resident macrophage ontogeny and homeostasis. *Immunity* 44, 439–449. <https://doi.org/10.1016/j.immuni.2016.02.024>.
- Goldin, R.D., Ratnayaka, I.D., Breach, C.S., Brown, I.N., and Wickramasinghe, S.N. (1996). Role of macrophages in acetaminophen (paracetamol)-induced hepatotoxicity. *J. Pathol.* 179, 432–435. [https://doi.org/10.1002/\(SICI\)1096-9896\(199608\)179:4<432::AID-PATH609>3.0.CO;2-S](https://doi.org/10.1002/(SICI)1096-9896(199608)179:4<432::AID-PATH609>3.0.CO;2-S).
- Halpern, K.B., Shenhav, R., Massalha, H., Toth, B., Egozi, A., Massasa, E.E., Medgalia, C., David, E., Giladi, A., Moor, A.E., et al. (2018). Paired-cell sequencing enables spatial gene expression mapping of liver endothelial cells. *Nat. Biotechnol.* 36, 962–970. <https://doi.org/10.1038/nbt.4231>.
- Halpern, K.B., Shenhav, R., Matcovitch-Natan, O., Tóth, B., Lemze, D., Golan, M., Massasa, E.E., Baydatch, S., Landen, S., Moor, A.E., et al. (2017). Single-cell spatial reconstruction reveals global division of labour in the mammalian liver. *Nature* 542, 352–356. <https://doi.org/10.1038/nature21065>.
- Harnik, Y., Buchauer, L., Ben-Moshe, S., Averbukh, I., Levin, Y., Savidor, A., Eilam, R., Moor, A.E., and Itzkovitz, S. (2021). Spatial discordances between mRNAs and proteins in the intestinal epithelium. *Nature Metabolism* 3, 1680–1693. <https://doi.org/10.1038/s42255-021-00504-6>.
- He, L., Pu, W., Liu, X., Zhang, Z., Han, M., Li, Y., Huang, X., Han, X., Li, Y., Liu, K., et al. (2021). Proliferation tracing reveals regional hepatocyte generation in liver homeostasis and repair. *Science* 371, eabc4346. <https://doi.org/10.1126/science.abc4346>.
- Henderson, N.C., and Iredale, J.P. (2007). Liver fibrosis: cellular mechanisms of progression and resolution. *Clin. Sci. (Lond)* 112, 265–280. <https://doi.org/10.1042/CS20060242>.
- Hentsch, B., Lyons, I., Li, R., Hartley, L., Lints, T.J., Adams, J.M., and Harvey, R.P. (1996). Hlx homeo box gene is essential for an inductive tissue interaction that drives expansion of embryonic liver and gut. *Genes Dev* 10, 70–79. <https://doi.org/10.1101/gad.10.1.70>.
- Hynes, R.O. (2009). The extracellular matrix: not just pretty fibrils. *Science* 326, 1216–1219. <https://doi.org/10.1126/science.1176009>.
- Inverso, D., Shi, J., Lee, K.H., Jakab, M., Ben-Moshe, S., Kulkarni, S.R., Schneider, M., Wang, G., Komeili, M., Vélez, P.A., et al. (2021). A spatial vascular transcriptomic, proteomic, and phosphoproteomic atlas unveils an angiocrine Tie-Wnt signaling axis in the liver. *Dev. Cell* 56, 1677–1693.e10. <https://doi.org/10.1016/j.devcel.2021.05.001>.
- Iwai, M., Morikawa, T., Muramatsu, A., Tanaka, S., Mori, T., Harada, Y., Okanoue, T., Kashima, K., and Ishii, M. (2000). Biological significance of AFP expression in liver injury induced by CCL₄. *Acta Histochem. Cytochem.* 33, 17–22. <https://doi.org/10.1267/ahc.33.17>.
- Jaitin, D.A., Adlung, L., Thaiss, C.A., Weiner, A., Li, B., Descamps, H., Lundgren, P., Blierot, C., Liu, Z., Deczkowska, A., et al. (2019). Lipid-associated macrophages control metabolic homeostasis in a Trem2-dependent manner. *Cell* 178, 686–698.e14. <https://doi.org/10.1016/j.cell.2019.05.054>.
- Jungermann, K., and Kietzmann, T. (1996). Zonation of parenchymal and non-parenchymal metabolism in liver. *Annu. Rev. Nutr.* 16, 179–203. <https://doi.org/10.1146/annurev.nu.16.070196.001143>.
- Kalucka, J., de Rooij, L.P.M.H., Goveia, J., Rohlenova, K., Dumas, S.J., Meta, E., Concinha, N.V., Taverna, F., Teuwen, L.-A., Veys, K., et al. (2020). Single-cell transcriptome atlas of murine endothelial cells. *Cell* 180, 764–779.e20. <https://doi.org/10.1016/j.cell.2020.01.015>.
- Karlmark, K.R., Weiskirchen, R., Zimmermann, H.W., Gassler, N., Ginhoux, F., Weber, C., Merad, M., Luedde, T., Trautwein, C., and Tacke, F. (2009). Hepatic recruitment of the inflammatory Gr1+ monocyte subset upon liver injury promotes hepatic fibrosis. *Hepatology* 50, 261–274. <https://doi.org/10.1002/hep.22950>.
- Kisseleva, T., and Brenner, D.A. (2006). Hepatic stellate cells and the reversal of fibrosis. *J. Gastroenterol. Hepatol.* 21, S84–S87. <https://doi.org/10.1111/j.1440-1746.2006.04584.x>.
- Kolodziejczyk, A.A., Federici, S., Zmora, N., Mohapatra, G., Dori-Bachash, M., Hornstein, S., Leshem, A., Reuveni, D., Zigmund, E., Tobar, A., et al. (2020). Acute liver failure is regulated by MYC- and microbiome-dependent programs. *Nat. Med.* 26, 1899–1911. <https://doi.org/10.1038/s41591-020-1102-2>.
- Kuhlmann, W.D. (1978). Localization of ALPHA1-fetoprotein and DNA-synthesis in liver cell populations during experimental hepatocarcinogenesis in rats. *Int. J. Cancer* 21, 368–380. <https://doi.org/10.1002/ijc.2910210319>.
- Liu, L.X., Lee, N.P., Chan, V.W., Xue, W., Zender, L., Zhang, C., Mao, M., Dai, H., Wang, X.L., Xu, M.Z., et al. (2009). Targeting cadherin-17 inactivates Wnt signaling and inhibits tumor growth in liver carcinoma. *Hepatology* 50, 1453–1463. <https://doi.org/10.1002/hep.23143>.
- Liu, X., Xu, J., Rosenthal, S., Zhang, L.J., McCubbin, R., Meshgin, N., Shang, L., Koyama, Y., Ma, H.-Y., Sharma, S., et al. (2020). Identification of lineage-specific transcription factors that prevent activation of hepatic stellate cells and promote fibrosis resolution. *Gastroenterology* 158, 1728–1744.e14. <https://doi.org/10.1053/j.gastro.2020.01.027>.
- Lu, Y., Liu, M., Yang, J., Weissman, S.M., Pan, X., Katz, S.G., and Wang, S. (2021). Spatial transcriptome profiling by MERFISH reveals fetal liver hematopoietic stem cell niche architecture. *Cell Discov.* 7, 1–17. <https://doi.org/10.1038/s41421-021-00266-1>.
- Lyubimova, A., Itzkovitz, S., Junker, J.P., Fan, Z.P., Wu, X., and van Oudenaarden, A. (2013). Single-molecule mRNA detection and counting in mammalian tissue. *Nature Protocols* 8, 1743–1758. <https://doi.org/10.1038/nprot.2013.109>.
- Macosko, E.Z., Basu, A., Satija, R., Nemes, J., Shekhar, K., Goldman, M., Tirosh, I., Bialas, A.R., Kamitaki, N., Martersteck, E.M., Trombetta, J.J., Weitz, D.A., Sanes, J.R., Shalek, A.K., Regev, A., and McCarroll, S.A. (2015). Highly Parallel Genome-wide Expression Profiling of Individual Cells Using Nanoliter Droplets. *Cell* 161, 1202–1214. <https://doi.org/10.1016/j.cell.2015.05.002>.
- Mak, K.M., and Png, C.Y.M. (2020). The hepatic central vein: structure, fibrosis, and role in liver biology. *Anat. Rec. (Hoboken)* 303, 1747–1767. <https://doi.org/10.1002/ar.24273>.
- Mederacke, I., Dapito, D.H., Affò, S., Uchinami, H., and Schwabe, R.F. (2015). High-yield and high-purity isolation of hepatic stellate cells from normal and fibrotic mouse livers. *Nature Protocols* 10, 305–315. <https://doi.org/10.1038/nprot.2015.017>.
- Michalopoulos, G.K., and DeFrances, M.C. (1997). Liver regeneration. *Science* 276, 60–66. <https://doi.org/10.1126/science.276.5309.60>.
- Monga, S.P. (2015). β -catenin signaling and roles in liver homeostasis, injury, and tumorigenesis. *Gastroenterology* 148, 1294–1310. <https://doi.org/10.1053/j.gastro.2015.02.056>.
- Moor, A.E., Harnik, Y., Ben-Moshe, S., Massasa, E.E., Rozenberg, M., Eilam, R., Bahar Halpern, K., and Itzkovitz, S. (2018). Spatial reconstruction of single enterocytes uncovers broad zonation along the intestinal villus axis. *Cell* 175, 1156–1167.e15. <https://doi.org/10.1016/j.cell.2018.08.063>.
- Mootha, V.K., Lindgren, C.M., Eriksson, K.-F., Subramanian, A., Sihag, S., Lehar, J., Puigserver, P., Carlsson, E., Ridderstråle, M., Laurila, E., Houstis, N., Daly, M.J., Patterson, N., Mesirov, J.P., Golub, T.R., Tamayo, P.,

- Spiegelman, B., Lander, E.S., Hirschhorn, J.N., and Groop, L.C. (2003). PGC-1 α -responsive genes involved in oxidative phosphorylation are coordinately downregulated in human diabetes. *Nature Genetics* 34, 267–273. <https://doi.org/10.1038/ng1180>.
- Mossanen, J.C., and Tacke, F. (2015). Acetaminophen-induced acute liver injury in mice. *Lab. Anim.* 49, 30–36. <https://doi.org/10.1177/0023677215570992>.
- Naba, A., Clauser, K.R., Ding, H., Whittaker, C.A., Carr, S.A., and Hynes, R.O. (2016). The extracellular matrix: tools and insights for the “omics” era. *Matrix Biol* 49, 10–24. <https://doi.org/10.1016/j.matbio.2015.06.003>.
- Nakamura, T., Nawa, K., and Ichihara, A. (1984). Partial purification and characterization of hepatocyte growth factor from serum of hepatectomized rats. *Biochem. Biophys. Res. Commun.* 122, 1450–1459. [https://doi.org/10.1016/0006-291X\(84\)91253-1](https://doi.org/10.1016/0006-291X(84)91253-1).
- Nakano, Y., Nakao, S., Sumiyoshi, H., Mikami, K., Tanno, Y., Sueoka, M., Kasahara, D., Kimura, H., Moro, T., Kamiya, A., et al. (2017). Identification of a novel alpha-fetoprotein-expressing cell population induced by the Jagged1/Notch2 signal in murine fibrotic liver. *Hepatology* 65, 215–229. <https://doi.org/10.1002/hep4.1026>.
- Newman, A.M., Steen, C.B., Liu, C.L., Gentles, A.J., Chaudhuri, A.A., Scherer, F., Khodadoust, M.S., Esfahani, M.S., Luca, B.A., Steiner, D., et al. (2019). Determining cell type abundance and expression from bulk tissues with digital cytometry. *Nat. Biotechnol.* 37, 773–782. <https://doi.org/10.1038/s41587-019-0114-2>.
- Otsu, N. (1979). A threshold selection method from gray-level histograms. *IEEE Trans. Syst. Man Cybern.* 9, 62–66. <https://doi.org/10.1109/TSMC.1979.4310076>.
- Parekh, S., Ziegenhain, C., Vieth, B., Enard, W., and Hellmann, I. (2018). zUMIs—A fast and flexible pipeline to process RNA sequencing data with UMIs. *GigaScience* 7. <https://doi.org/10.1093/gigascience/giy059>.
- Pellicoro, A., Ramachandran, P., Iredale, J.P., and Fallowfield, J.A. (2014). Liver fibrosis and repair: immune regulation of wound healing in a solid organ. *Nat. Rev. Immunol.* 14, 181–194. <https://doi.org/10.1038/nri3623>.
- Planas-Paz, L., Orsini, V., Boulter, L., Calabrese, D., Pikiólek, M., Nigsch, F., Xie, Y., Roma, G., Donovan, A., Marti, P., et al. (2016). The RSPO-LGR4/5-ZNRF3/RNF43 module controls liver zonation and size. *Nat. Cell Biol.* 18, 467–479. <https://doi.org/10.1038/ncb3337>.
- Poisson, J., Lemoine, S., Boulanger, C., Durand, F., Moreau, R., Valla, D., and Rautou, P.-E. (2017). Liver sinusoidal endothelial cells: physiology and role in liver diseases. *J. Hepatol.* 66, 212–227. <https://doi.org/10.1016/j.jhep.2016.07.009>.
- Preziosi, M., Okabe, H., Poddar, M., Singh, S., and Monga, S.P. (2018). Endothelial Wnts regulate β -catenin signaling in murine liver zonation and regeneration: A sequel to the Wnt-Wnt situation. *Hepatology* 67, 845–860. <https://doi.org/10.1002/hep4.1196>.
- Puche, J.E., Saiman, Y., and Friedman, S.L. (2013). Hepatic stellate cells and liver fibrosis. *Compr. Physiol.* 3, 1473–1492.
- Ramilowski, J.A., Goldberg, T., Harshbarger, J., Kloppmann, E., Lizio, M., Satagopam, V.P., Itoh, M., Kawaji, H., Carninci, P., Rost, B., and Forrest, A.R.R. (2015). A draft network of ligand–receptor-mediated multicellular signalling in human. *Nat. Commun.* 6, 7866. <https://doi.org/10.1038/ncomms8866>.
- Recknagel, R.O. (1967). Carbon tetrachloride hepatotoxicity. *Pharmacol. Rev.* 19, 145–208.
- Remmerie, A., Martens, L., Thoné, T., Castoldi, A., Seurinck, R., Pavie, B., Roels, J., Vanneste, B., De Prijck, S., Vanhockerhout, M., et al. (2020). Osteopontin expression identifies a subset of recruited macrophages distinct from Kupffer cells in the fatty liver. *Immunity* 53, 641–657. e14. <https://doi.org/10.1016/j.immuni.2020.08.004>.
- Ruoslahti, E., and Seppälä, M. (1979). α -fetoprotein in cancer and fetal development. In *Advances in Cancer Research*, 29, G. Klein and S. Weinhouse, eds. (Academic Press), pp. 275–346. [https://doi.org/10.1016/S0065-230X\(08\)60849-0](https://doi.org/10.1016/S0065-230X(08)60849-0).
- Schiodt, F.V., Ostapowicz, G., Murray, N., Satyanarana, R., Zaman, A., Munoz, S., and Lee, W.M. (2006). Alpha-fetoprotein and prognosis in acute liver failure. *Liver Transpl.* 12, 1776–1781. <https://doi.org/10.1002/lt.20886>.
- Schmidt, L.E., and Dalhoff, K. (2005). Alpha-fetoprotein is a predictor of outcome in acetaminophen-induced liver injury. *Hepatology* 41, 26–31. <https://doi.org/10.1002/hep.20511>.
- Schneider, C.A., Rasband, W.S., and Eliceiri, K.W. (2012). NIH Image to ImageJ: 25 years of image analysis. *Nature Methods* 9, 671–675. <https://doi.org/10.1038/nmeth.2089>.
- Schwahnhäuser, B., Busse, D., Li, N., Dittmar, G., Schuchhardt, J., Wolf, J., Chen, W., and Selbach, M. (2011). Global quantification of mammalian gene expression control. *Nature* 473, 337–342. <https://doi.org/10.1038/nature10098>.
- Sharma, A., Seow, J.J.W., Dutertre, C.-A., Pai, R., Blériot, C., Mishra, A., Wong, R.M.M., Singh, G.S.N., Sudhagar, S., Khalilnezhad, S., et al. (2020). Onco-fetal reprogramming of endothelial cells drives immunosuppressive macrophages in hepatocellular carcinoma. *Cell* 183, 377–394. e21. <https://doi.org/10.1016/j.cell.2020.08.040>.
- Singh, S., Hynan, L.S., Rule, J.A., and Lee, W.M. (2019). Changes in alpha-fetoprotein and Gc-globulin in relation to outcomes in non-acetaminophen acute liver failure. *Liver Int* 39, 2368–2373. <https://doi.org/10.1111/liv.14216>.
- Stoeckius, M., Zheng, S., Houck-Loomis, B., Hao, S., Yeung, B.Z., Mauck, W.M., Smibert, P., and Satija, R. (2018). Cell Hashing with barcoded antibodies enables multiplexing and doublet detection for single cell genomics. *Genome Biology* 19, 224. <https://doi.org/10.1186/s13059-018-1603-1>.
- Stuart, T., Butler, A., Hoffman, P., Hafemeister, C., Papalexi, E., Mauck, W.M., Hao, Y., Stoeckius, M., Smibert, P., and Satija, R. (2019). Comprehensive Integration of Single-Cell Data. *Cell* 177, 1888–1902. e21. <https://doi.org/10.1016/j.cell.2019.05.031>.
- Subramanian, A., Tamayo, P., Mootha, V.K., Mukherjee, S., Ebert, B.L., Gillette, M.A., Paulovich, A., Pomeroy, S.L., Golub, T.R., Lander, E.S., and Mesirov, J.P. (2005). Gene set enrichment analysis: A knowledge-based approach for interpreting genome-wide expression profiles. *Proceedings of the National Academy of Sciences* 102, 15545–15550. <https://doi.org/10.1073/pnas.0506580102>.
- Sun, T., Annunziato, S., Bergling, S., Sheng, C., Orsini, V., Forcella, P., Pikiólek, M., Kancharla, V., Holwerda, S., Imanci, D., et al. (2021). ZNRF3 and RNF43 cooperate to safeguard metabolic liver zonation and hepatocyte proliferation. *Cell Stem Cell* 28, 1822–1837. e10. <https://doi.org/10.1016/j.stem.2021.05.013>.
- Sun, T., Pikiólek, M., Orsini, V., Bergling, S., Holwerda, S., Morelli, L., Hoppe, P.S., Planas-Paz, L., Yang, Y., Ruffner, H., et al. (2020). AXIN2+ Pericentral Hepatocytes Have Limited contributions to liver homeostasis and regeneration. *Cell Stem Cell* 26, 97–107. e6. <https://doi.org/10.1016/j.stem.2019.10.011>.
- Tacke, F., and Zimmermann, H.W. (2014). Macrophage heterogeneity in liver injury and fibrosis. *J. Hepatol.* 60, 1090–1096. <https://doi.org/10.1016/j.jhep.2013.12.025>.
- Tanami, S., Ben-Moshe, S., Elkayam, A., Mayo, A., Bahar Halpern, K., and Itzkovitz, S. (2017). Dynamic zonation of liver polyploidy. *Cell Tissue Res.* 368, 405–410. <https://doi.org/10.1007/s00441-016-2427-5>.
- Tipton, D.A., and Dabbous, M.K. (1998). Autocrine transforming growth factor β stimulation of extracellular matrix production by fibroblasts from fibrotic human gingiva. *J. Periodontol.* 69, 609–619. <https://doi.org/10.1902/jop.1998.69.6.609>.
- Troeger, J.S., Mederacke, I., Gwak, G.Y., Dapito, D.H., Mu, X., Hsu, C.C., Pradere, J.P., Friedman, R.A., and Schwabe, R.F. (2012). Deactivation of hepatic stellate cells during liver fibrosis resolution in mice. *Gastroenterology* 143, 1073–1083. e22. <https://doi.org/10.1053/j.gastro.2012.06.036>.
- Van de Sande, B., Flerin, C., Davie, K., De Waegeneer, M., Hulselmans, G., Aibar, S., Seurinck, R., Saelens, W., Cannoodt, R., Rouchon, Q., et al. (2020). A scalable SCENIC workflow for single-cell gene regulatory network analysis. *Nat. Protoc.* 15, 2247–2276. <https://doi.org/10.1038/s41596-020-0336-2>.

Wang, B., Zhao, L., Fish, M., Logan, C.Y., and Nusse, R. (2015). Self-renewing diploid Axin2 + cells fuel homeostatic renewal of the liver. *Nature* 524, 180–185. <https://doi.org/10.1038/nature14863>.

Wang, G., Chen, S., Zhao, C., Li, X., Zhang, L., Zhao, W., Chang, C., and Xu, C. (2016). Gene expression profiles predict the possible regulatory role of OPN-mediated signaling pathways in rat liver regeneration. *Gene* 576, 782–790. <https://doi.org/10.1016/j.gene.2015.11.008>.

Wei, Y., Wang, Y.G., Jia, Y., Li, L., Yoon, J., Zhang, S., Wang, Z., Zhang, Y., Zhu, M., Sharma, T., et al. (2021). Liver homeostasis is maintained by midlobular zone 2 hepatocytes. *Science* 371. eabb1625. <https://doi.org/10.1126/science.abb1625>.

Werb, Z., and Gordon, S. (1975). Elastase secretion by stimulated macrophages. Characterization and regulation. *J. Exp. Med.* 142, 361–377. <https://doi.org/10.1084/jem.142.2.361>.

Xiong, X., Kuang, H., Ansari, S., Liu, T., Gong, J., Wang, S., Zhao, X.Y., Ji, Y., Li, C., Guo, L., et al. (2019). Landscape of intercellular crosstalk in healthy and

NASH liver revealed by single-cell secretome gene analysis. *Mol. Cell* 75, 644–660.e5. <https://doi.org/10.1016/j.molcel.2019.07.028>.

Yanger, K., Knigin, D., Zong, Y., Maggs, L., Gu, G., Akiyama, H., Pikarsky, E., and Stanger, B.Z. (2014). Adult hepatocytes are generated by self-duplication Rather than stem cell differentiation. *Cell Stem Cell* 15, 340–349. <https://doi.org/10.1016/j.stem.2014.06.003>.

Zhao, L., Jin, Y., Donahue, K., Tsui, M., Fish, M., Logan, C.Y., Wang, B., and Nusse, R. (2019). Tissue repair in the mouse liver following acute carbon tetrachloride depends on injury-induced Wnt/ β -catenin signaling. *Hepatology* 69, 2623–2635. <https://doi.org/10.1002/hep.30563>.

Zigmond, E., Samia-Grinberg, S., Pasmanik-Chor, M., Brazowski, E., Shibolet, O., Halpern, Z., and Varol, C. (2014). Infiltrating monocyte-derived macrophages and resident Kupffer cells display different ontogeny and functions in acute liver injury. *J. Immunol.* 193, 344–353. <https://doi.org/10.4049/jimmunol.1400574>.

STAR★METHODS

KEY RESOURCES TABLE

REAGENT or RESOURCE	SOURCE	IDENTIFIER
Antibodies		
TruStain fcX (anti-mouse CD16/32) Antibody	Biolegend	Cat#101320; RRID: AB_1574975
TotalSeq™-B0303 anti-mouse Hashtag 3 Antibody	Biolegend	Cat# 155805; RRID: AB_2750034
TotalSeq™-B0304 anti-mouse Hashtag 4 Antibody	Biolegend	Cat# 155807; RRID: AB_2750035
TotalSeq™-B0305 anti-mouse Hashtag 5 Antibody	Biolegend	Cat# 155809; RRID: AB_2750036
TotalSeq™-B0306 anti-mouse Hashtag 6 Antibody	Biolegend	Cat # No. 155841; RRID: AB_2814072
TotalSeq™-B0307 anti-mouse Hashtag 7 Antibody	Biolegend	Cat# 155813; RRID: AB_2750039
TotalSeq™-B0308 anti-mouse Hashtag 8 Antibody	Biolegend	Cat# 155815; RRID: AB_2750040
Biological samples		
BSA, nuclease-free, 50 mg ml ⁻¹	Ambion	Cat# AM2616
Chemicals, peptides, and recombinant proteins		
Alexa Fluor™ 488 Phalloidin	Thermo Fisher	Cat# A12379
6-Carboxytetramethylrhodamine succinimidyl ester (TMR)	Molecular probes	Cat# C6123
Cy5 succinimidyl ester	GE Healthcare	Cat# PA25001
Alexa Fluor 594 carboxylic acid succinimidyl ester	Thermo Fisher	Cat# A37572
Formaldehyde, 37% (w/v)	J.T. Baker	Cat# JT2106
Formamide, deionized, nuclease-free	Ambion	Cat# AM9342
O.C.T. Compound Cryostat Embedding Medium	Scigen	Cat# 4586
Pronase	Roche	11459643001
Collagenase D	Roche	11088866001
Liberase™ TL Research Grade	Roche	5401020001
Red blood cell lysis buffer Hybri-Max	Sigma	Cat# R7757
Percoll	Sigma	Cat# P1644
Cell staining buffer	BioLegend	Cat #420201
Acetaminophen	Merck	CAS# 103-90-2
Ketavet	Zoetis Manufacturing & Research	N/A
Sedaxylan	EuroVet	Vm# 16849/4001
Critical commercial assays		
10x Single Cell 3' Reagent Kits v3.1 Chemistry with Feature Barcoding technology for Cell Surface Protein	10x Genomics	N/A
Visium Spatial Gene Expression	10x Genomics	N/A
Direct-Zol™ RNA MiniPrep	Zymo Research	Cat# R2052
Qubit™ dsDNA HS Assay Kit	invitrogen	Cat# Q32851
Agilent High Sensitivity D1000	Agilent Technologies	5067- 5584 5067- 5585
Nextera XT DNA Library Prep Kit	Illumina	Cat# FC-131-1024
NextSeq 500 Kits v2 (75 cycles)	Illumina	Cat# FC-404-2005
NovaSeq 6000 SP Reagent Kit (100 cycles)	Illumina	Cat# 20027464
Deposited data		
single cell transcriptomics of mouse liver cells at different time points after APAP ip injection	This paper	Zenodo. DOI: https://doi.org/10.5281/zenodo.6035873

(Continued on next page)

Continued

REAGENT or RESOURCE	SOURCE	IDENTIFIER
Spatial transcriptomics of mouse liver slides at different time points after APAP ip injection	This paper	Zenodo. DOI: https://doi.org/10.5281/zenodo.6035873
Bulk mRNAseq of mouse livers at different time points after APAP ip injection	This paper	Zenodo. DOI: https://doi.org/10.5281/zenodo.6035873
Single cell RNAseq of control hepatocytes (ZT0A, ZT0B)	Droin et al., 2021	GSE145197
Single cell RNAseq of control and 20h after APAP injection HSCs (SPF_1, SPF_2, SPF_3, SPF_APAP_1, SPF_APAP_2, SPF_APAP_3, SPF_APAP_4)	Kolodziejczyk et al., 2020	ArrayExpress
Fetal liver cells scRNAseq data (E14.5FL)	Lu et al., 2021	GSE172127
Experimental models: Organisms/strains		
C57BL/6 inbred mice	Envigo	Strain: C57BL/6JOLAHsd
Oligonucleotides		
smFISH probes (see Table S12)	This paper	Table S12
Software and algorithms		
R 4.1.2 and R studio	R Consortium	https://www.rstudio.com/
Matlab 2018b	MathWorks®	https://www.mathworks.com/
Python v3.9	Python	https://www.python.org/
Bcl2Fastq v2.20.0.422	Illumina	https://emea.support.illumina.com/downloads/bcl2fastq-conversion-software-v2-20.html
zUMIs v0.0.4	Parekh et al., 2018	https://github.com/sdparekh/zUMIs
Cell ranger 3.1.0	10x Genomics	https://support.10xgenomics.com/single-cell-gene-expression/software/downloads/latest
Space ranger	10x Genomics	https://support.10xgenomics.com/spatial-gene-expression/software/downloads/latest
Seurat	Butler et al., 2018	https://satijalab.org/seurat/
Nichnet	Browaeys et al., 2020	https://github.com/saeyslab/nichenetr
SCENIC	Aibar et al., 2017 ; Van de Sande et al., 2020	https://scenic.aertslab.org/
CIBERSORTx	Newman et al., 2019	https://cibersortx.stanford.edu/
Stellaris FISH Probe Designer	Biosearch Technologies	http://singlemoleculefish.com/
GSEA	Subramanian et al., 2005 ; Mootha et al., 2003	https://www.gsea-msigdb.org/gsea/index.jsp
ImageJ	Schneider et al., 2012	https://imagej.nih.gov/ij/

RESOURCE AVAILABILITY

Lead contact

Further information and requests for resources and reagents should be directed to and will be fulfilled by the lead contact, Shalev Itzkovitz (shalev.itzkovitz@weizmann.ac.il).

Materials availability

The study did not generate new unique reagents.

Data and code availability

- All sequencing data have been deposited at Zenodo repository and are publicly available under the following URL: <https://doi.org/10.5281/zenodo.6035873>. DOI is also listed in the [key resources table](#).
- Data can also be browsed in our webapp: <https://itzkovitzapapp.weizmann.ac.il/apap/> Spatial-temporal dynamics of genes can be plotted in both scRNAseq and spatial transcriptomics datasets. Datasets are also available to download from the webapp.
- All codes used in this paper are available from the [lead contact](#) upon request.
- Any additional information required to reanalyze the data reported in this paper is available from the [lead contact](#) upon request.

Data generated in this study available at the Zenodo repository under the following URL: <https://doi.org/10.5281/zenodo.6035873>. Data can also be browsed in our webapp: <https://itzkovitzapapp.weizmann.ac.il/apap/>. Spatial temporal dynamics of genes can be plotted in both scRNAseq and spatial transcriptomics datasets. Datasets are also available to download from the webapp.

All codes used in this paper, as well as any additional information required to reanalyze are available from the [lead contact](#) upon request.

EXPERIMENTAL MODEL AND SUBJECT DETAILS

Mouse experiments were approved by the Institutional Animal Care and Use Committee of the Weizmann Institute of Science and were conducted in agreement with the institute guidelines. Male (C57BL/6J01aHsd) mice aged 8–11 weeks, housed under regular 12h light-dark cycle, were used in our experiments. Food (Teklad Global 18% Protein Rodent Diet) was taken out 12h prior to APAP injection. Mice had access to drinking water. A dose of 300mg/1kg body weight of APAP (Merck, 103-90-2), dissolved in saline 0.9%, was injected i.p at a concentration of 40mg/ml. APAP solution was slightly heated to improve drug solubility. In order to avoid circadian rhythm effects, all timepoints were carried out at the same hour of the day – food was taken out at ZT16 (10pm) and APAP or saline was injected at ZT4 (10am). Food was given back to mice after injection mice were fed ad libitum until sacrificed for experiment.

For bulk RNA sequencing and smFISH experiments, 8 control mice were injected with saline alone following 12h fasting – at 6h, 24h, 96h and 1m, 2 mice per time point. Mice were injected with APAP 6h, 24h, 48h, 72h, 96h, 1week and 1month prior to their sacrifice, 3 mice per time point. For scRNAseq experiments, non-injected mice were used as controls (n=2) and mice were injected with APAP 24h (n=2), 48h (n=4), 72h (n=2), 96h (n=3) and 1week (n=2) prior to their sacrifice.

METHODS DETAILS

Single molecule fluorescence in-situ hybridization (smFISH)

APAP- or saline- treated mice were sacrificed 6h, 24h, 48h, 72h, 96h, 1w and 1m after injection. Mice were sacrificed by cervical dislocation. A part of the median lobe was taken for bulk mRNA sequencing, and the rest of the liver was fixed with pre-chilled 4% PFA for 3h in 4°C followed by an overnight incubation with 4% PFA and 30% sucrose in 4°C. Fixed liver was then embedded in OCT. smFISH experiments were performed on 8µm thick cryosections mounted on poly-L-lysine pre-coated coverslips. Probe libraries were designed using the Stellaris FISH Probe Designer Software (Biosearch Technologies, Inc., Petaluma, CA). Hybridization was performed according to published protocol (Lyubimova et al., 2013). Briefly, tissues were permeabilized for 10min with proteinase K (10µg/ml Ambion AM2546) followed by 2 washes of 2× SSC (Ambion AM9765) for 5min. Tissues were incubated in wash buffer (20% Formamide Ambion AM9342, 2× SSC) for 5min and then with hybridization buffer (10% Dextran sulfate Sigma D8906, 20% Formamide, 1mg/ml E.coli tRNA Sigma R1753, 2× SSC, 0.02% BSA Ambion AM2616, 2 mM Vanadylribonucleoside complex NEB S1402S) mixed with probes. Hybridization mix was incubated with tissues overnight in a 30°C incubator. smFISH probe libraries were coupled to Cy5, TMR or Alexa594. Table S7 includes a list of all the probe sequences used in this study. After the hybridization, tissues were washed with wash buffer containing 50ng/ml DAPI for 30 min at 30°C. DAPI (Sigma-Aldrich, D9542) was used for nuclear staining. Membranes were labeled using actin filaments staining by Phalloidin (ThermoFisher). All images were performed on a Nikon-Ti-E inverted fluorescence microscope using the NIS element software AR 5.11.01. Scans spanning from central to portal veins were acquired using 100x magnification. Stitching of the individual fields was done by NIS element program, with 15% overlap.

Library construction for bulk liver mRNA

Mice injected with APAP or saline vehicle only were sacrificed using cervical dislocation. A small part from the median liver lobe, between 2–5mm³, was taken for bulk RNA sequencing, and the rest of the organ was fixed for smFISH experiments, as aforementioned. Tissue samples were placed in cold 600µl TRI-reagent for RNA isolation (Sigma). 0.5mm diameter RNase free zirconium-oxide homogenization beads (Next Advance) were added in a mass comparable to that of the tissue sample, and samples were homogenized in a Bullet Blender (Next Advance) using speed 8 setting for 3mins. After the homogenization step, samples were centrifuged (14,000 rpm, 30sec) and 500µl from the supernatant were transferred into a new Eppendorf tube. An equal volume of 100% EtOH was added to the sample. From that tube, 500µl of sample were transferred into Direct-zol RNA miniprep column (Zymo research). RNA extraction was performed as detailed in kit protocol, with a DNase I incubation step. Total RNA was eluted in 20µl nuclease free water and 1µl of total RNA was taken for library construction. Libraries were prepared according to mcSCRbseq protocol (Bagnoli et al., 2018). Following reverse transcription and exo-nuclease steps, cDNA was pre-amplified with 10–15 cycles, depending on cDNA concentration, indicated by qPCR quality control. 2ng of the amplified cDNA were used to library construction, using Nextera XT DNA Library kit (Illumina, FC-131-1024), according to manufacturer protocol. Quality control of the resulting libraries was performed with an Agilent High Sensitivity D1000 ScreenTape System (Agilent, 5067- 5584). Libraries were loaded with a concentration of 2.2pM on 75 cycle high output flow cells (Illumina, FC-404-2005) and sequenced on a NextSeq 500/550 (Illumina) with the following cycle distribution: 8bp index1, 16 bp read1, 66 bp read2 (no index2 needed), with estimated depth of 15M reads per sample. A total of 29 libraries for 29 different mice were sequenced.

Data processing for bulk mRNA

Illumina output files were demultiplexed with bcl2fastq v.2.17. Resulting FASTQ files were analyzed using the zUMIs pipeline (Parekh et al., 2018). Reads were aligned with STAR (v.2.5.3a) to the GRCm38 genome (release 84; Ensembl) and exonic unique molecular identifier (UMI) counts were used for downstream analysis. Two samples (CT_24h_m9 and CT_24h_m10) were discarded for having a total UMI sum of less than 1.5M UMIs. Data was further normalized by dividing each sample by its sum of UMIs, resulting in normalized expression levels corresponding to the gene's fraction in the sample.

Principal component analysis on bulk samples

Fractions were natural-log transformed (after the addition of the minimal fraction larger than zero) and Z-scores of the log transformed fractions of each gene were calculated across all samples. PCA was calculated on the Z-scores. In order to avoid circadian effects, control mice which were injected with saline 6h prior to the experiment were discarded from the pool of control mice.

Liver perfusions and hepatocyte dissociation

Mice were anaesthetized with 100 mg/kg Ketamine (Zoetis Manufacturing & Research) and 10 mg/kg Xylazine (EuroVet) dissolved in 1 × PBS and injected i.p. Once anaesthetized, their livers were perfused as previously described (Mederacke et al., 2015), with some adjustments. A 27 G syringe connected to perfusion line and pump was inserted into the vena cava; 7-10 ml of pre-warmed to 37 °C EGTA buffer were perfused to wash the blood from the liver. After EGTA, 12-20 ml of pre-warmed to 37 °C enzyme buffer solution (EBS) with 2.3 U of Liberase (Roche) were cannulated into the vena cava to isolate hepatocytes. Shortly after the beginning of the perfusion, the portal vein was cut to allow drainage of the blood. Successfully perfused livers were extracted to a Petri dish with 25 ml of pre-warmed EBS and gently minced using forceps. Dissociated liver cells were collected and filtered through a 100µm cell strainer. Cells were spun down at 30g for 3 min at 4 °C to obtain the hepatocyte-enriched pellet. Pellet was resuspended in 25ml cold EBS. To enrich for live hepatocytes, 22.5 ml Percoll (Sigma-Aldrich) mixed with 2.5 ml 10× PBS was added to the cells. Cells were centrifuged at 600 rpm for 10min at RT. The supernatant containing the dead cells was aspirated and cells were resuspended in Cell Staining Buffer (BioLegend).

Liver perfusions of non-parenchymal cell (NPC)

Perfusion procedure for NPC dissociation was similar to that of hepatocytes, although it required the use of different dissociating enzymes. Instead of using Liberase Blendzyme 3, livers were sequentially perfused with 7-10ml 37°C EGTA, then 10-15 ml of pre-warmed to 37 °C enzyme buffer solution (EBS) containing 0.4 mg/ml Pronase protease (Roche) and then with 15-20 ml of 37 °C EBS containing collagenase D (0.1 U/ml) (Roche). Damaged livers (48h-72h after APAP injection) were perfused with 1.5x concentration of dissociating enzymes. Livers were extracted to a Petri dish with 25 ml of pre-warmed EBS and gently minced using forceps. Dissociated liver cells were filtered through a 70µm cell strainer. Cells were spun down at 30g for 3 min at 4 °C twice, and each time the pellet was discarded to eliminate the hepatocytes. Supernatant was then centrifuged at 580g for 10min in 4°C. Pellet containing NPCs was resuspended in 1ml Red Blood Cell Lysis Buffer (Sigma), incubated at room temp for 1min at RT. EBS was then added and samples were centrifuged again in 580g for 10min in 4°C. Pellet was resuspended in 100-200µl Cell Staining Buffer (BioLegend).

TotalSeq™-B for 10x feature barcoding

We multiplexed our samples using a hashing technique (Stoeckius et al., 2018) by labeling samples with oligonucleotide-barcoded antibodies. To this end, we used commercial tagged antibodies - TotalSeq™-B for 10x Feature Barcoding (BioLegend), according to manufacturer protocol. A small fraction of the cells was stained with 50% trypan blue to validate that dead cells do not make up more than 25% of the sample. Hepatocytes / NPCs were counted and 2M cells in a volume of 100µl Cell Staining Buffer were taken for further preparation. Cells from each mouse were blocked with 5µl of FCX (BioLegend) for 10min in 4°C. While cells were incubating in blocking solution, Total seq B antibodies (BioLegend) were prepared using 1µg of each TotalSeq™ hashtag antibody. Unique antibodies were then added to each sample and were incubated for 30min in 4°C. To wash out the antibodies, samples were filled to 10ml with Cell Staining Buffer and centrifuged 500g in 4°C for 5 minutes 3 times. Finally, cells were counted and cells viability was estimated using trypan blue, to make sure no more than 30% cells of the samples are dead.

Single cell libraries with feature barcoding

Two to four antibody-tagged hashed samples were multiplexed into one well of 10x Chromium Next GEM Chip G, loading approximately 10,000 cells per well (2,500-5,000 cells per sample). Single cells were processed using the 10x Chromium Next GEM Single Cell 3' Reagent Kits v3.1 with Feature Barcoding technology for Cell Surface Protein, according manufacturer's manual. Libraries were sequenced using NovaSeq 6000 using NovaSeq Sp (100 cycles) sequencing Kits (Illumina). A total of 7 sequencing runs of cells taken from 19 mice: 15 mice for NPC (2 non injected control mice, 2mice 20h after APAP, 4mice 48h after APAP, 2mice 72h after APAP, 3mice 96h after APAP and 2mice 1w after APAP), and 4 mice for hepatocytes (2mice for 48h after APAP and 2mice for 72h after APAP).

Single-cell RNAseq data analysis

Single-cell RNA-seq data were demultiplexed, aligned to the GRCm38 mouse genome assembly (mm10) and UMIs were quantified using the Cell Ranger Single-Cell Software Suite 3.1.0 and bcl2fastq, with the functions "cellranger mkfastq" and "cellranger count".

Data pre-processing and background subtraction

Starting from the raw matrix output of Cell Ranger, droplets with low counts of UMIs were filtered out. Threshold was set to 1,000 UMIs, however, in sequencing runs with a 99.9th quantile of sum of UMIs of below 1000, threshold was reduced to 500 UMIs. Of the remaining droplets, sum of UMIs for each droplet were \log_{10} -transformed, and Otsu's method (Otsu, 1979) was used to determine a threshold that separates empty from cell-containing droplets (Macosko et al., 2015). Cells were defined as droplets with \log_{10} UMI sums above this threshold. Background was defined as droplets with \log_{10} UMI sums below the threshold. These droplets potentially contained floating RNA from dead or ruptured cells. The mean UMI count of each gene across the background droplets was calculated. This vector was subtracted from each cell. The same averaging and subtraction were performed for UMI counts of the feature barcodes. Negative values were corrected to zero. This background subtraction was done independently for each sequencing run.

Data processing of NPCs using Seurat package

Background-subtracted cells' gene expression matrices were further analyzed using the R package Seurat 3.1.5 (Stuart et al., 2019). Cells with UMI sums of above 3,000 UMIs and mitochondrial gene percent less than 15% were retained. Only cells with maximal fraction of feature barcode above 70% were included, to avoid doublets. Genes detected in a minimum of 5 cells were retained. Data were normalized and scaled using the SCTransform function, with regression of sum of UMIs (`vars.to.regress = "nCount_RNA"`). PCA was calculated based on the variable genes found in the previous function, however, mitochondrial ("[^]mt-") and ribosomal ("[^]Rp[lsj]") genes were manually removed from the gene list since they are prone to batch-related expression variability. Following PCA, number of PCs for clustering was determined using the elbow plot method (between 15-20 PCs). Clustering was performed with default parameters. Resulting clusters were then manually annotated after extracting cluster markers using FindAllMarkers Seurat function. Clusters containing more than 50% cells with expression of markers of more than one cell type (for example cluster of cells expressing both HSC marker *Dcn* and Kupffer cell marker *Clec4f*) were removed and remaining cells were retransformed, re-clustered and re-annotated.

Data integration of NPCs

Seurat objects from all sequencing runs were integrated using the following Seurat functions: 'SelectIntegrationFeatures', with mitochondrial and ribosomal genes excluded from the output 5,000 genes; 'PrepSCTIntegration' with default settings; and 'FindIntegrationAnchors' and 'IntegrateData' with 'SCT' as the normalization method. PCA and clustering on integrated Seurat object was done as detailed above for the individual Seurat objects. Clusters were annotated to the main liver resident / infiltrating immune cell types: endothelial cells, HSC, hepatocytes, cholangiocytes, Kupffer cells (KC), monocytes, macrophages, plasmacytoid dendritic cells (pDC), conventional dendritic cells (cDC), B cells, T cells and natural killer (NK) cells.

Hepatocyte processing

Our experimental data included hepatocytes from two mice sacrificed at 48 hours and two mice at 72 hours after APAP injection, dissociated using Liberase enzyme. In order to include control non-injected hepatocytes, hepatocytes from a previously published study (Droin et al., 2021) were integrated. Notably, the animals were held at the same facility prior to experiment as animals used for our experiments and cells isolation and library construction were performed similarly to the APAP experiments. From their data set, the two mice perfused at a similar circadian time as our mice (samples 'ZT6A' and 'ZT6B') were chosen. Fatsq files of these two mice were re-aligned and preprocessed as detailed above for our sequencing runs, to eliminate any bioinformatics biases. Individual Seurat objects were created for the two mice, filtering out cells with less than 1,000 total UMI count and with mitochondrial percentage of less than 9% and more than 35%, as was found to capture viable hepatocytes (Droin et al., 2021). These included 923 cells for ZT6A and 1,076 cells for ZT6B. Next, we created a Seurat object of our background-removed APAP-injected hepatocytes to include cells with UMI count of at least 2,500 UMIs and mitochondrial percent of 9%-35% with fraction of maximal feature barcode above 70%. Doublets were removed from the dataset after clustering, as described above for NPCs. The Seurat object included 532 hepatocytes from 2 mice 48h after APAP injection, and 239 hepatocytes from 2 mice 72h after APAP injection.

Data integration of hepatocytes

Integration of control mice and APAP injected mice was performed in the same manner as for NPCs. In total, 2770 cells from either control, 48h or 72h after APAP injection time points were used for hepatocyte analysis. Integrated hepatocyte cluster was then integrated with NPC clusters, using the same integration parameters described above.

Finding markers for different cell types

To plot the heatmap of differentially expressed genes between the different cell types (Figure S1A), a signature matrix containing the mean normalized expression of the genes in each of the 11 cell type clusters was computed. The matrix included only genes with maximal normalized mean expression above 5×10^{-4} . Our markers for each cell type included genes for which the expression was highest for the respective cell and more than 2-fold higher than any other cell type. We further retained for each cell type, the 8 genes with the highest ratio as markers.

Estimating cellular composition using CIBERSORTx

To avoid biases originating in dissociation and sensitivity differences between the different cell types, we imputed the abundance of each of the 11 main cell types found in our scRNAseq dataset in each of the time points after APAP injection in our bulk samples using

CIBERSORTx computational deconvolution software (Newman et al., 2019). To this end, the “impute cell fractions” module of the online tool was used, with the bulk liver RNAseq dataset of 17,972 genes expressed in 29 bulk liver samples as the mixture file. The mean expression per cell type in our single cell data was used for the signature matrix. First, expression of each cell was normalized to the cell’s sum of UMI counts, resulting in expression fractions. Next, the mean expression of genes was calculated for each cell type. The resulting matrix of 19,344 genes across 11 cell types was the input for the signature matrix file. CIBERSORTx was executed with the default parameters (Table S2B).

Temporal dynamics of KEGG pathways

KEGG pathway analysis of the bulk RNAseq data (Figure S1C) was performed as follows: the expression of each gene was normalized by division by the maximal expression level across the eight time points. Then, the max-normalized expressions of genes comprising each KEGG pathway were grouped and the mean expression was calculated for each time point. Those means were further normalized to the maximal mean-expression across all time point for each pathway. Max normalization was performed to eliminate effects of expression levels between different genes and of gene set sizes between different pathways. Relevant KEGG pathways were manually selected for display and sorted by the time of their peak expression.

Extracting hepatocyte temporal changes

To follow the temporal changes of hepatocytes throughout the liver regeneration time course (Figure 2A), bulk liver RNAseq data was used. First, hepatocyte specific genes were selected by detecting genes with mean expression level of at least 10^{-4} and 20-fold higher in the hepatocyte cluster in the scRNAseq dataset than any of the other 10 cell type clusters. Mup genes were excluded from the list of genes, given their high variability. Next, 328 out of the resulting 342 hepatocyte specific genes were found in the bulk RNAseq dataset. Each gene was further normalized by dividing the sum of the 328 genes in each sample. Spearman correlation was then calculated between the normalized expression of these genes for all pairs of four control samples (not including 6h control due to circadian differences and 24h controls, due to insufficient coverage) and APAP-treated samples.

Visium 10x spatial transcriptomics

APAP treated mice were sacrificed 24h, 48h and 72h after injection (2 mice per time point). Mice were sacrificed by cervical dislocation. Liver tissues were washed with 1x PBS and embedded in OCT. Tissues were sectioned into 10 μ m thick slices and placed on Visium tissue optimization or spatial gene expression slides (10x genomics). Tissues were fixed with methanol and stained with H&E according to the Visium staining user guide. H&E images were taken on Leica Widefield-DMI8 microscope with 20x magnification. Tissues were permeabilized for 30 minutes, based on initial optimization trials. Libraries were prepared according to the Visium Spatial Gene Expression User guide with 16 cycles of PCR for cDNA amplification and 12 cycles for the sample index PCR (Dual Index Kit TT Set A, 10X Genomics, PN-1000215). Libraries were pooled, loaded at a concentration of 400pM and sequenced on a NovaSeq 6000 SP100 flow cell.

Fastq reads from the Illumina sequencer NovaSeq 6000 were preprocessed by 10X Genomics spaceranger-1.3.0 software including spatial de-barcoding, read-alignment to mm10 and UMI-generation.

Spatial transcriptomics processing

Number of UMIs, fraction of mitochondrial genes and fraction of hemoglobin genes ($^{\wedge}$ Hb[ab]-) were calculated for each spot. Spots with hemoglobin fraction of over 1% were removed. Spots with total UMI count of under four standard deviations from UMI count mean across all spots, calculated for each slide individually, were further filtered out. Similarly, spots with fraction of mitochondrial genes surpassing four standard deviations above slide mean were excluded. Those filtrations were aimed at removing bad quality spots, as well as spots localized in blood vessels and not overlaying cells. Next, spots localized at the outer layers of the tissue, manually annotated as spots distanced up to 2 spots from tissue edges, were removed from analysis.

The remaining spots were used for analysis. UMI counts were normalized by dividing each count to the spot’s UMI sum, resulting in fractions of UMIs. To analyze the spatial context, the fibrogenic signature of each spot was calculated by the fraction of the collagen genes ($^{\wedge}$ Col[1-9]) in each spot. Spots with over one standard deviation above slide mean were annotated as fibrotic spots. Since collagens localize to the pericentral zones 48h and 72h after APAP injection, these spots were set as the pericentral tissue coordinates. Since at 24h after APAP injection collagens are not yet sufficiently elevated, pericentral necrotic regions were manually segmented in the two liver slides taken 24h after injection using Loupe Browser (10x Genomics). All annotations were further manually validated to ensure they do not include areas of portal myofibroblasts. The area of each connected fibrotic/necrotic region was then reduced into a skeleton curve as follows (Figure S2). We computationally overlaid a rectangular grid over the Visium hexagonal grid. This essentially amounts to adding intervening spots to the existing hexagonal grid at every other row and column. We then annotated a rectangular grid location as ‘fibrotic’ if it contained at least two fibrotic spots within a distance of 85 μ m on the original hexagonal grid (where spots are 100 μ m apart). Finally, the Matlab skeletonization function was applied on the rectangular grid, to obtain the pericentral core. Each spot was assigned a distance from the nearest pericentral skeleton curve. All spots up to 350 μ m from the nearest skeleton curve were binned into three equal groups based on their distances. Those groups represented the pericentral zone, the mid-lobule zone and the periportal zone.

Inferring lobule spatial coordinates of single hepatocytes

Several studies have established algorithms for computationally inferring the spatial coordinates of dissociated single cells (Achim et al., 2015; Droin et al., 2021; Halpern et al., 2017, 2018; Moor et al., 2018). Expression of known zoned genes, termed landmark genes, provides spatial information about the origin of the hepatocyte, along the one-dimensional porto-central axis. Due to the substantial transcriptional changes that hepatocytes undergo in the course of APAP-induced damage and regeneration, we utilized our spatial transcriptomics measurements to identify landmark genes that are consistently zoned across all time points. To this end, two sets of pericentral and periportal hepatocyte landmark genes for control livers were first extracted based on Halpern et al. (Halpern et al., 2017), a paper that provides average hepatocyte gene expression over 9 lobule layers spanning the porto-central axis. These genes had maximal normalized expression above 1×10^{-5} across all lobule layers, fold change higher than 10% between the most pericentral and periportal layers and mean ratio between standard error and mean across all layers lower than 0.2 (to discard highly variable genes). This initial filtration resulted in 2,535 pericentral and 1,656 periportal landmark gene candidates.

Next, this list of candidate landmark genes was examined over the Visium datasets of the APAP-treated livers. In order to reflect the zonation in expression of only hepatocytes, the expression at each spot was re-normalized over a subset of hepatocyte-specific genes. These were defined as genes with hepatocyte expression above 10^{-5} and 5-fold higher expression in hepatocytes compared to any of the remaining 10 cell type clusters in our scRNAseq dataset. The mean and standard error of each of these renormalized hepatocyte specific genes was calculated for each of the three zones in each of the six Visium slide. Next, a list of potential landmark genes was extracted for each slide, using the same filtration criteria used for the control data. For Visium slides, an additional filtration removed genes expressed in less than 20% of the hepatocyte-containing spots. A final list of genes passing the filtration criteria both in control and in each of the six Visium slides was used as landmark genes. These included 33 pericentral landmark genes and 58 periportal landmark genes (Table S3A).

The pericentral and periportal landmark genes underwent two-step normalization (Halpern et al., 2018): first, the genes were divided by the sum of total UMI count of each cell, to reflect the fraction of expression of each landmark gene in each hepatocyte. Second, the genes were scaled by dividing them by their maximal expression across all hepatocytes. This provided similar weight to all landmark genes, regardless of expression levels differences among them. Then, for each cell, the sum of normalized-scaled levels of all central landmark genes (cLM) and of all portal landmark genes (pLM) was computed. The computational zonation coordinate was defined as $pLM / (cLM + pLM)$. Cells were equally assigned to the three discrete zones – pericentral (or peri-necrotic), mid-lobule or periportal, zonation coordinates were sorted for each time point based on percentiles. To extract zonation profiles of genes at different time points (Table S3B), the means and standard errors of the means were calculated for cells from same time point and zone.

Analyzing proliferation in hepatocytes

Analysis of proliferation at different zones and time points was done using smFISH. Liver sections of mice 32h, 40h, 48h and 72h post APAP injection were hybridized with *Mki67* smFISH probes. Liver lobules sections were scanned (at least 5 scans per mouse, 2 mice per time points). All hepatocytes in the porto-central axis scan were counted and were labeled as *Mki67* positive if they had more than 2 smFISH dots. The distances of each hepatocyte to the central vein and the portal vein were calculated using Euclidean distances, and a zonation coordinate was given to each hepatocyte, calculated as the distance to the central vein divided by the sum of distances to the central vein and the portal vein. Cells were next classified into one of three zones – pericentral/perinecrotic, mid-lobule and periportal, based on their zonation coordinate. For every scan, the fraction of dividing cells ($\#Mki67$ positive hepatocytes / $\#$ total hepatocytes) was calculated. For each time point, Kruskal-Wallis test was performed to assess differential proliferation between the zones (Figure 2I).

Comparing proliferating and non-proliferating hepatocytes

To identify differences between proliferating and non-proliferating hepatocytes, hepatocytes from each zone and each time point were classified to either dividing (non-zero expression of *Mki67* in the scRNAseq dataset) or non-dividing (zero expression of *Mki67*). Differential expression analysis was done per zone, to eliminate spatial biases. The Fold-change of the mean gene expression between the *Mki67* positive and negative hepatocytes in each zone at 48h and 72h post APAP injection, as well as the Kruskal-wallis p-value and the FDR q-values are reported in Table S3C. For a general analysis, a global comparison between *Mki67* positive and negative hepatocytes in the regenerating tissues was also computed. Genes were ranked by their \log_2 fold-change of expression between the two groups, and GSEA was performed, using the KEGG and Hallmark genesets (Figure S3F).

Comparing interface hepatocytes and control

Interface hepatocytes were defined as hepatocytes assigned to the most pericentral zone in the respective time point (namely, third of the cells with the most pericentral spatial coordinate in each time point). In order to compare pericentral/peri-necrotic hepatocytes at 48h and 72h post APAP injection with control pericentral hepatocytes, there is a need to validate that cells sampled from both time points are from similar lobule coordinates. Since during APAP damage and regeneration most pericentral layers of hepatocytes are lost, the remaining central-most hepatocytes are from the peri-necrotic region, which in control mice, would not be comparable to the most pericentral layers, but rather to the central-mid layers. Therefore, to conserve similarity in spatial coordinate distributions in control and regenerating hepatocytes, 100 control hepatocytes were randomly sampled to match the distribution of zonation coordinates of the APAP-injected pericentral hepatocytes in each of the two time points. This was done using the inverse transform sampling method (Devroye, 2006). The mean expression of the sampled cell was then compared against the mean expression of the interface hepatocytes.

Gene Set Enrichment Analysis (GSEA) of interface hepatocytes

To identify gene pathways enriched in interface hepatocytes, Spearman correlations of genes with the expression of *Afp*, which was found to be specifically expressed in interface cells, were calculated. Cells included in this analysis were only from 48h and 72h after APAP injection and from pericentral and mid-lobule zones, where interface hepatocytes were detected. Next, the top 99th percentile genes with the highest correlation with *Afp* (108 genes) from each of the two time points were summed up and the Spearman correlation of individual genes with this meta-signature was calculated. Included in this analysis were genes, with mean sum-normalized expression higher than 5×10^{-6} in at least one time point. The list of the remaining genes was ranked by their Spearman correlation and was used as input in GSEA tool, for preranked genes (Mootha et al., 2003; Subramanian et al., 2005). Gene list was analyzed against KEGG and Hallmark gene sets datasets.

Measuring length of porto-central axes

H&E images of control and 1 week after APAP (2 mice per time point) were scanned and the distances of central veins to their closest portal triads were measured. In total, 59 lobules from control mice and 62 lobules from 1 week after APAP injection were measured. Kruskal-Wallis test was performed to check significance of lobule size differences.

Measuring nucleus diameter of hepatocytes

H&E images of control, 1 week after APAP and 1 month after APAP were scanned. In total 1,518 hepatocytes were analyzed. Peri-central and periportal populations were defined as the two adjacent hepatocyte layers surrounding the vein. The nuclear diameter was measured by Case Viewer software. The diameters of the nuclei were matched to ploidy levels sizes was based on previous study (Tanami et al., 2017).

Hepatic stellate cell cluster analysis

The integrated cluster of HSCs included 465 cells from 4 mice 48h after APAP injection, 98 cells from 2 mice 72h, 31 cells from 96h and 78 cells from 1w after APAP injection. However, our sequencing experiments failed to capture sufficient numbers of cells from control and 24h after APAP injection. To complement the dataset, we used a recently published dataset (Kolodziejczyk et al., 2020). Again, the animals were held at the same facility prior to experiment as animals used for our experiments and cells isolation and library construction were done in a similar manner to ours. Nonetheless, in this study, APAP injection was given to non-fasted mice in a concentration of 500mg/Kg and cells were sorted prior to loading on 10x chromium. We used seven wt mice: three non-treated mice ('SFP_1', 'SPF_2', and 'SPF_3' mice) and four mice injected with APAP 20h prior to perfusion ('SFP_APAP_1', 'SPF_APAP_2', 'SPF_APAP_3', and 'SPF_APAP_2'). Fatsq files of these seven mice were re-aligned and preprocessed as detailed above for our sequencing runs, to eliminate any bioinformatics biases. Individual Seurat objects were created for the seven mice, filtering out cell with less than 3,000 total UMI count and with mitochondrial percentage of more than 15%. The Seurat objects were then integrated as described above and clusters of HSC (annotated by markers found using 'FindAllMarkers' function) were subset. These included 563 cells from 3 control mice and 1,073 cells from 4 mice 20h after APAP injection. Next, we integrated HSC from our experiments and from Kolodziejczyk et al. using same integration method described above. The few cells from 24h after APAP from our measurements were pooled with cells from 20h after APAP. Overall, HSC cluster included 2,311 HSCs from six pooled time points.

Inferring lobule spatial coordinates of single HSCs

Unlike hepatocytes, the transcriptomes of which dominate individual Visium spots, liver non-parenchymal transcriptomes were highly diluted in each spot, preventing similar robust detection of landmark genes with this approach. As an alternative, we based our landmark gene extraction on smFISH validations of a known landmark gene. Zonation of quiescent and activated HSCs was previously studied (Dobie et al., 2019). *Ngfr* was found to be highly correlated with periportal and pericentral zonation, respectively (Dobie et al., 2019). Given the notable transcriptional changes induced by liver damage and HSC activation, smFISH was used to validate that *Ngfr* was consistently expressed at higher levels in periportal genes. *Ngfr* was therefore used as our main periportal landmark gene. Due to the low capture rate and dropouts associated with scRNAseq, we sought to increase the number of landmark genes for each time point. To this end, single-cell Spearman correlations of each gene with *Ngfr* were calculated, for each time point separately. Expression levels were normalized to the sum of UMI count for each cell. Only genes with mean expression levels over all cells in the specific time point higher than 10^{-4} and correlation higher than 0.25 were considered for first iteration. This yielded a signature of six periportal genes appearing in at least five out of the six time points: *Ngfr*, *Plvap*, *Colec11*, *Sod3*, *Steap4* and *Ifitm1*. In a second iteration, the correlation of each gene with the summed expression level of these six periportal landmark genes was calculated. For each time point, genes with mean expression higher than 10^{-4} and Spearman correlation higher than 0.4 or lower than -0.4 and correlation p-value lower than 0.01 were considered as landmark genes – positively correlated genes as portal landmark genes and negatively correlated genes as central landmark genes. Mitochondrial ('^mt-') and ribosomal ('^Rp[ls]') genes were excluded from all landmark gene lists. After establishing the portal and central landmark genes for each time point, further analysis and zone assignment were performed as described above for hepatocytes.

Spatio-temporal analysis of the matrisome

The gene sets of the matrisome (Naba et al., 2016) were analyzed in a similar way to the temporal dynamics of KEGG pathways described above. Max-normalized expression of the genes from the same matrisome gene set were averaged over single HSC from each lobule layer and at each time point.

Ligand-target interaction analysis of activated HSC

Nichenet (Browaeys et al., 2020) was used to elucidate which cellular interaction correlate with HSC activation. To focus on the activation process, HSC genes which were upregulated in pericentral HSCs at 20h/24h or 48h after APAP injection compared to control pericentral HSCs were extracted as the target up-regulated gene set. To this end, differential expression analysis was performed between single pericentral control HSCs and pericentral HSCs from either 20h or 48h after APAP injection. Only genes whose mean expression level was higher than 10^{-5} and were present in at least 5% of the cells in either of the compared groups were included. Among these, genes with a fold-change of at least 2 and q-value below 10^{-10} were maintained. These two lists of genes (one for 20h/24h and one for 48h) were compared against background lists containing all genes expressed in pericentral HSC in the respective time points with a mean of over 10^{-5} . The input list of potentially active ligands (Figures S6D and S6E) was filtered by our bulk mRNAseq dataset. Only ligands upregulated compared to control bulk samples with a fold change of at least 2 and with expression level of over 10^{-6} at the corresponding time points were maintained. Using Nichenet, the top 50 ligands with highest activity were predicted for pericentral HSCs at 24h and 48h after APAP. The sum of activities of each ligand with all its targets was calculated. Top 20 ligands with the highest sum of activities were presented for each time point in Figures S6D and S6E.

Endothelial cell cluster analysis

Integrated cluster of endothelial cells was comprised of 6,527 cells, 978 cells from 2 control mice, 654 cells from 2 mice 24h after APAP injection, 1,234 cells from 2 mice 48h after APAP injection, 1,229 cells from 2 mice 72h after APAP injection, 797 cells from 3 mice 96h after APAP injection and 1,635 cells from 2 mice 1 week after APAP injection.

Inferring lobule spatial coordinates of single endothelial cells

Spatial variability of endothelial cells is originating from both the location along the lobule porto-central and from the endothelial cell subtype – either liver vascular endothelial cells (LVECs), or liver sinusoidal endothelial cells (LSEC) (Kalucka et al., 2020). Endothelial cells were thus divided into five zonated populations: pericentral (PC-) LVEC, PC-LSEC, mid-lobule (mid) LSEC, periportal (PP-) LSEC and PP-LVEC. The endothelial cells were first subset into a separate Seurat object, reclustered using Seurat. Clusters expressing the vascular endothelial cell marker *Vwf* (Kalucka et al., 2020) were annotated as LVEC clusters. Of those, the cluster expressing both *Vwf* and *Wnt2*, a prominent pericentral marker (Halpern et al., 2018; Wang et al., 2015), was annotated as PC-LVEC and the remaining cluster was annotated as PP-LVEC.

Next, the zonation of LSEC was computed. We curated a list of landmark genes for each of our time point in a similar fashion to HSCs. The genes *Dll4*, *Msr1*, *Clec4g*, *Sox17* and *Efm2* were used as initial periportal landmark genes in all time points. Spearman correlations of each gene with the summed expression level of these five periportal landmark genes were calculated. For each time point, genes with mean expression higher than 10^{-5} and correlation higher than 0.2 or lower than -0.2 and correlation pval lower than 0.01 were considered as portal or central landmark genes, respectively. Mitochondrial ([^]mt-) and ribosomal ([^]Rp[ls]) genes were excluded from all landmark gene lists. After establishing the portal and central landmark genes for LSECs in each time point, further analysis and zone assignment of LSECs were performed as described above for hepatocytes and HSCs.

Validations of spatial reconstruction using spatial transcriptomics dataset

The Visium data was used to validate the zonation profiles of hepatocytes, HSCs and endothelial cells that were computationally inferred based on single cells at the different time points. To this end we compared the single cell reconstruction zonation profiles for zonated genes, defined as genes with a normalized expression level of at least 10^{-5} in at least one zone, with significant zonated expression (FDR < 0.05) and a dynamic range of at least 2-fold difference between the pericentral and the periportal zones. For endothelial cells the dynamic range requirement considered PP-LSEC vs. PC-LSEC, rather than LVEC. Each Visium spot contains multiple cell types, and expression patterns could therefore be confounded by differential zonal representation of distinct cell types. To correct for this, cell-type specific gene expression values were computed for each cell types. To this end, the scRNAseq data was used to compute the mean expression values over all of the 11 cell types. The cell-type specific genes were defined as genes with maximal expression above 5×10^{-6} , and 5-fold higher expression over any other cell type. Additionally, for HSCs and endothelial cells genes were required to be expressed at a value lower than 10^{-5} in hepatocytes. Upon extraction of cell-type specific genes, UMI values were divided by the sum of all UMI values of all cell-type specific genes. Only genes appearing in more than 5% of the spots in each slide were included. The dynamic range of the genes was then calculated for the Visium dataset in the same manner as for the scRNAseq data, and the dynamic ranges by scRNAseq spatial reconstruction were compared with the dynamic ranges of each of the Visium slide in the respective time point. Spearman correlations were calculated for the log₂-transformed dynamic ranges (Figures S2H–S2J).

Identifying putative transcription factors upstream of Hgf

Gene regulatory network analysis was performed using the SCENIC tool (version 0.11.2) with default parameters (Van de Sande et al., 2020). In order to control for the different abundances of the cell types, scRNAseq dataset was first randomly subset to include up to

500 cells from each cell type at each time point. Adjacency matrix for each transcription factor (TF) and targets in our dataset, as well as area under the curve (AUC) scores of each TF per each cell were computed and used for downstream analyses.

To identify transcription factors associated with expression of *Hgf* in HSCs and endothelial cells, differential analysis was done by comparing the AUC scores between HSCs/endothelial cells with *Hgf* expression level above 10^{-4} and HSCs/endothelial cells with *Hgf* expression level below 10^{-4} . The Fold-change of the mean AUC for each of the 213 TFs detected by SCENIC between the *Hgf* positive and negative cells, as well as the Kruskal-wallis p-val and the FDR values are reported in [Table S4C](#).

Myeloid clusters analysis

The integrated NPC dataset included 9,338 cells in five main myeloid clusters: Kupffer cells, monocytes, macrophages, pDCs and cDCs. These cells were subset to a separate Seurat object, and cells were processed and clustered as detailed for the individual sequencing runs. 10 PCs were used for clustering, and resolution was set to 0.2. Markers for each of the resulting 10 clusters were found using 'FindAllMarkers' function, and clusters were subsequently annotated to different cell types and cell states, using ImmGen database (available at <http://www.immgen.org/>) and previous studies ([Deczkowska et al., 2021](#); [Kolodziejczyk et al., 2020](#)).

GSEA of activated Kupffer cells and macrophages

GSEA was then performed on a gene list ranked by the \log_2 of ratio between the mean expression of genes in activated Kupffer cells cluster over 24h, 48h and 72h after APAP injection, and the mean of cells from macrophages and Ly6c- monocyte clusters from the same time points. Enrichment was calculated against the Hallmark dataset with default parameters.

Interaction analysis from scRNAseq dataset

Ligand-receptor pairs were taken from a previously published dataset ([Ramilowski et al., 2015](#)). Expression of genes was averaged for each of the 11 cell type and each of the six time point. Hepatocytes, endothelial cells and HSCs were further sub-clustered into their spatially resolved zones, resulting in total of 19 cell type sub-clusters. An interaction matrix was generated by crossing receptors from all cell-types with their respective ligands in all cell types at each time point. Namely, we crossed all the receptors expressed in each cell type at each time point, with matching ligands expressed at all other cell types at that time point, including self-interaction (ligand and receptor both expressed at the same cell type). Ligand-receptor pairs with expression level of over 10^{-5} fraction of UMIs in either ligand or receptor were retained. Interaction potential was calculated as the multiplication of the expression levels of the ligands and receptors. In addition, the fold change of each ligand and receptor from the levels in control mice were also calculated. The resulted matrix is presented in [Table S6](#).

Interaction analysis from spatial transcriptomics dataset

Ligand-receptor interactions were also investigated in the spatial-transcriptomics dataset. Ligand-receptor pairs in each Visium slide were analyzed. Spearman correlation of each ligand-receptor pair expression was calculated, either for across all slide spots, or for each of the three stratified lobule zones (discretized by growing distances from the central cores). In addition to correlations, interaction potential was also calculated as the mean product of the expression of the ligand and receptor over all spots, either across the whole slide, or across each zone. The results are summarized in [Table S5](#).

Comparing regenerating cells with fetal datasets

A previously published scRNAseq dataset of mouse fetal liver was parsed and annotated ([Lu et al., 2021](#)). In order to control for the different experimental settings of our dataset and the fetal liver dataset, both datasets were first normalized to adult control.

Spatially different sub-clusters of hepatocytes and endothelial cells were compared against their matched control population. Fetal macrophages, as well as regenerating KCs were compared against control adult KCs. Genes included in the differential expression analysis were genes that had at least 10^{-5} expression fraction and were expressed in at least 5% of the cells in either one of the two compared groups. The Spearman correlations of the fold change of the fetal and each of the respective regenerating populations from control was calculated and the correlation coefficients are presented in [Figure S4](#).

QUANTIFICATION AND STATISTICAL ANALYSIS

Quantification and statistical analysis are detailed above for each of the different analyses performed. In general, Kruskal-Wallis tests were used to infer statistical differences. When multiple hypotheses were applied, a subsequent Benjamini-Hochberg False Discovery Rate (FDR) q-value was also calculated, to adjust the p-values obtained for single measurements. Spearman correlations were calculated. Gene expression fold change between two different cell populations was calculated as the \log_2 of the ratio between the two groups, with an addition of the minimal value bigger than 0 in both the numerator and denominator, to avoid division by 0.

ADDITIONAL RESOURCES

A web browser to explore the spatio-temporal dynamics of genes of interest: <https://itzkovitzapapp.weizmann.ac.il/apap/>.